Università degli Studi di Padova

Dipartimento di Fisica e Astronomia "Galileo Galilei"

Master degree in Astrophysics and Cosmology

FINAL DISSERTATION

Distribution of stellar rotational velocities in star clusters of the Magellanic Clouds

Supervisor:
Prof.ssa Paola Marigo

Candidate:
Greta Ettorre

Co-supervisors:
Prof. Léo Girardi
Dr. Alessandro Mazzi

Academic Year 2022/2023

”Hier kommt die Sonne
Sie ist der hellste Stern von allen”

Contents

List of Figures

List of Tables

Abstract

There has been growing evidence in recent years that star clusters in the Magellanic Clouds (MCs) contain stars with a significant spread in rotation velocity. Indeed, the Hubble Space Telescope (HST)'s excellent photometry has revealed new surprises, such as the presence of structures that cannot be represented by evolutionary isochrones for a single age or metallicity in the observed Colour-Magnitude Diagrams (CMD) of young and intermediate-age MCs clusters. These include the identification of extended main-sequence turn-offs (eMSTO) and split Main Sequence (MS), as well as instances of clusters with a dual Red Clump (RC). The "stellar rotation scenario", which attributes these CMD features to stellar rotation, is currently one of the most favored hypotheses.

In this thesis, I investigate the distribution of stellar rotation within four MCs clusters: NGC 419 of the Small Magellanic Cloud (SMC) and NGC 2203, NGC 1831, and NGC 1866 of the Large Magellanic Cloud (LMC). These clusters are densely populated with stars and exhibit all of the intriguing rotational features in their CMDs. The primary goal of this analysis is to explore how stellar rotation influences the morphology of CMDs and to retrieve the distribution of stellar rotational velocities of our target clusters using evolutionary models that include rotation and are complete in both evolutionary phases and color modeling. Using isochrones derived from PARSEC V2.0 stellar tracks and TRILEGAL, the analysis begins by generating distinct stellar populations, each with a different rotation rate. Using the *sfhfinder*, these populations, referred to as "Partial Models," are combined to create the final model, denoted as **M**. Optimization with gradient descent with momentum and Monte Carlo Markov Chain (MCMC) are used in this process, allowing **M** to represent the relative importance of each population corresponding to specific rotational velocities.

For each cluster I constructed 11 Partial Models (corresponding to 11 initial rotation velocities) and ran the analysis for 2 metallicites and 8 age values, yielding a total of 16 best-fitting models. The best model from among these 16 is chosen by computing and minimizing the Poissonian Likelihood Ratio, which takes into account the poissonian nature of our data distribution.

Furthermore, I used *sfhfinder* to fit the binary fraction, as well as magnitude and color shifts, for each cluster. Among the objects in this study, NGC 419 has the highest count of binary systems ($f_{\rm bin} = 0.200$), while NGC 1866 has the lowest count ($f_{\rm bin} = 0.085$).

Following the fitting procedure, the magnitude and color shifts are used to calculate the resulting distance and extinction. The calculated distance of the clusters is slightly greater than the assumed value, and the V-band extinction is also higher than the reference value, with the exception of NGC 1866.

According to the analysis, the rotational velocity distributions in all four clusters are peaked at high rotation rates and clearly reveal stars with $\omega_{\rm i} \gtrsim 0.6$. As a result, the CMD morphology of young and intermediate-age MCs clusters can be completely explained within the context of rapid and extreme rotation.

This research could be expanded to young and intermediate-age clusters within the Milky Way (MW) in the future, providing a more comprehensive understanding of the underlying mechanisms shaping CMDs in a different galactic environment.

The first chapter of this thesis provides an overview of the occurrence of multiple population phenomenon and multiple sequences within the CMDs of stellar clusters. The physics of stellar rotation and its effects on the CMDs are described in Chapter 2. The third chapter contains a brief description of each target cluster and outlines the adopted parameters such as age, metallicity, distance, and extinction as sourced from existing literature. The analysis methodology is outlined in Chapter 4. I present my results in the fifth chapter and draw my conclusions in the sixth chapter.

Chapter 1

Simple and Multiple stellar populations in star clusters

1.1 Simple stellar populations

Simple stellar populations (SSPs) consist of stars that were born from the same gas cloud at the same time and have a consistent chemical composition. This means that all stars within an SSP should have the same initial metal content and age. However, detailed observations of SSPs are only available for resolved stellar populations, such as Galactic clusters or star clusters in nearby galaxies. Indeed, star clusters are the closest objects to SSPs.

At any given age, single stars within an SSP form an isochrone in the theoretical Hertzsprung-Russell (HR) diagram, which can be transformed into an observational colour-magnitude diagram (CMD) by using atlas of stellar spectra that are calibrated in terms of flux, effective temperature, and metal content. To compute population synthesis models, a complete set of stellar evolutionary tracks is necessary. These tracks describe the evolution in the HR diagram of stars with different masses and metal contents. By interpolating a set of stellar tracks at a given time, we can build isochrones in the theoretical HR diagram. Since we know from stellar evolution theory that the main sequence lifetime of low-mass stars is longer with respect to more massive stars, it follows that the initial stellar mass increases along an isocrone, as we go to more advanced evolutionary phases. The number of stars at each position along the isochrone is determined by the assumed initial mass function (IMF), which specifies how many stars are born per interval of initial mass, or, in other words, it describes the probability distribution function for the initial mass of stars in a given population. The main regions that can be distinguished along an isochrone are the following ones:

- Main sequence (MS): in this phase stars are burning hydrogen (H) into helium (He).

- Turn-off (TO): it is the exact point in which stars exhaust the H in their core. Its position is a proxy of the age of the stellar population.
- Sub-giant Branch (SGB): Stars burn H in a shell around an inert He core.
- Red-giant Branch (RGB): the electrons in the He core become degenerate.
- Horizontal Branch (HB) or Red Clump (RC) depending on its effective temperature: He is burning in the core.
- Asymptotic Giant Branch (AGB): stars have two burning shells: one for H and one for He.

Historically, open clusters (OCs) were considered the best examples of young SSPs in nature. This assumption was supported by state-of-the-art CMDs where the photometric sequences of young clusters were similar to single isochrones, with some scattered stars which can be explained as binaries. An OC is a group of up to a few thousand stars that were formed from the same giant molecular cloud and have roughly the same age. They are loosely bound by mutual gravitational attraction and become disrupted by close encounters with other clusters and clouds of gas, for these reasons OCs generally survive for a few hundred million years, with the most massive ones surviving for a few billion years.

On the other side Globular Clusters (GCs) were thought to be the best examples of old SSPs. As outlined by Gratton et al. (2019), GCs are usually described as a class of stellar agglomerates characterized by being compact (half-light radius up to few tents of pc, with more typical values of about 3 to 5 pc), bright (mean absolute visual magnitude around $M_V = -7$), old ($\sim$ 10 Gyr), and (at least within the MW) to be representative of the halo, thick disk and bulge, but being absent in the thin disk.

One of the key features of their CMDs is the well-defined MS extending from the TO to fainter magnitudes and redder colours. Furthermore, contrary to open clusters, they show well-populated SGB and RGB, which is easily explained by stellar evolution theory: in the case of younger stellar populations stars evolve very fast away from the main sequence resulting in a smaller number of stars in the SGB, while in case of old populations these sequences are more rich in stars.

1.2 Multiple stellar populations

For many years star clusters were believed to form out of single star formation bursts, hence having the same age and chemical composition. In the last decades a strong improvement was achieved thanks to the Hubble Space Telescope (HST), and better computational facilities. This made it possible to study in a deeper way the CMDs of star clusters and realize that these stellar systems host multiple stellar populations, making the presence of more than one population in star clusters one of the most important discoveries in this field in recent years. Moreover, the acknowledgement of the

presence of different stellar populations with different chemical compositions and properties was also possible thanks to new photometric tools that are effective to maximize their separation. **Two-colour diagrams** involving far-UV, UV, and optical filters are widely used to identify multiple populations along different evolutionary phases. The most used ones are the F275W - F336W vs. F336W - F438W from the HST. The reason why these filters are efficient tools to identify MPs in GCs is that F275W and F336W passbands include OH and NH molecular bands, while F438W comprises CN and CH bands. These kind of diagrams are effective in discerning populations with different abundances of C, O and N. To investigate multiple populations along all evolutionary sequences together, Milone et al. (2013) combined colours to define the pseudo-colours, as for example $C_{\rm F275W,F343W,F438W}$ = (F275W - F343W)-(F343W-F438W). Starting from them, **pseudo colour-magnitude diagrams** are built, together with the analogous diagram made with ground-based photometry in U, B, and I bands. The **Chromosome Map** (ChM) is a pseudo-two-colour diagram that is built for MS, RGB, or AGB, separately. The main difference with a simple two-colour diagram is that the sequences of MS, RGB, or AGB stars are verticalized in both dimensions in such a way that stars of each stellar population are clustered in a small area of the ChM. The traditional ChMs are built by combining the F275W-F814W colour, which is mostly sensitive to helium variations, with the $C_{\rm F275W,F343W,F438W}$, which is mainly a proxy for nitrogen abundance. Examples of the previously described photometric tools are represented in Figure 1.1.

The growing evidence of multiple populations being present in globular clusters was mainly supported by three observational facts:

- Chemical anomalies: the chemical composition of their stars is not homogeneous in the elements associated with H-burning. Usually stars with Galactic-field-like chemical composition are called *first population* (1P), while stars enriched in He, N, Na, and Al and depleted in C and O define one or more following stellar populations, called *second population* (2P).
- The Second Parameter of the HB : clusters with similar metallicity show different HB morphology.
- Multiple Sequences in the CMDs: there has been growing evidence of split or broad MSs, RGBs, SGBs and broad MSTOs in the CMDs.

Recently, studies on M4 (Marino et al. (2008) and Marino et al. (2011)) revealed that all these three observational evidences are different sides of the same phenomenon, that is the *multiple population (MP) phenomenon*. Understanding this phenomenon and its origin is a challenge for stellar evolution theory and the mechanism behind star formation at high redshift.

Currently, it is still not clear what is the origin of this phenomenon, however few formation scenarios have been proposed. According to some scenarios the MPs correspond to stars with different age, hence born from different star formation events. In these sce-

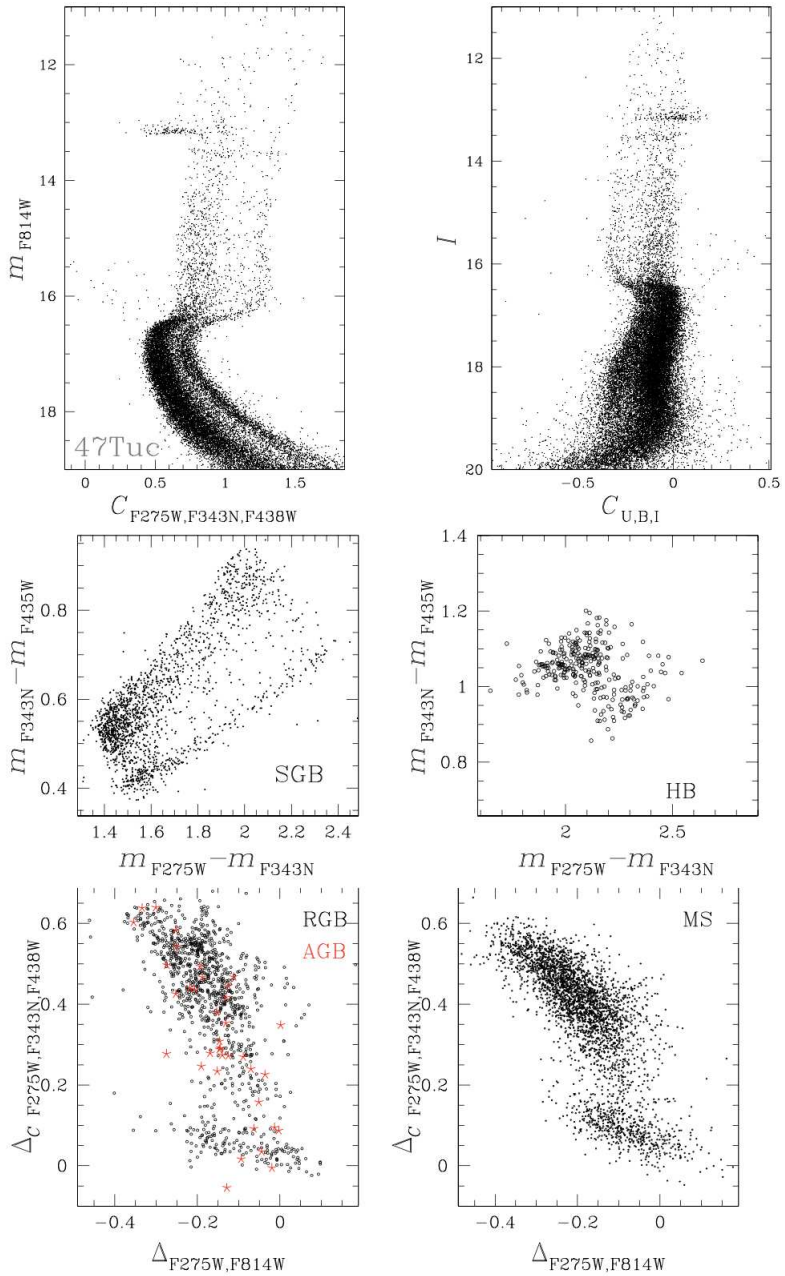

Figure 1.1: Collection of photometric diagrams to identify multiple populations in 47 Tucanae by Milone and Marino (2022). The top panels show the so-called "pseudo CMDs" which are CMDs constructed with combinations of different filters. Middle panels represent the "two colour diagrams" for the SGB and HB evolutionary phases. Bottom panels are the "Chromosome maps" in which the position of each star is indicative of its chemical composition.

narios, 2P stars would form from the gas polluted by more massive 1P stars. One of the most crucial consequences of this kind of scenarios is the so-called *mass-budget problem*: in order to account for the the large amount of 2P stars observed in present-day GCs, it is necessary that the progenitors of today's GCs were considerably more massive. As a consequence, these massive proto-GCs may have contributed to the cosmic reionization. Examples of these scenarios are "The Asymptotic Giant Branch Scenario" proposed by D'Ercole et al. (2008), which identifies AGB stars ejecting material with low-velocity winds as the polluters, and the "Fast-Rotating Massive Stars Scenario" by Decressin et al. (2007), according to which 2P stars originate from the gravitational instability in disks formed around massive stars expelling material with equatorial winds.

On the other side, it has also been suggested that MPs form in a single burst, with a fraction of stars being polluted by the ejecta of more massive stars of the same generation. According to this scenario the peculiar chemical composition of 2P raises from accretion phenomena that occur during the pre-MS phase. One of the most famous examples of this scenario is " The Super-Massive-Star Scenario", suggested by Denissenkov and Hartwick (2013), which states that the abundance anomalies of proton-capture elements in GCs are produced by Supermassive Stars with $M \sim 10^4\ M_{\odot}$.

1.3 Multiple sequences in young and intermediate age star clusters

Most Galactic GCs with multiple populations are ancient stellar systems, older than $\sim 11-12$ Gyr. On the other side, the analysis of open clusters of the Milky Way (MW) reveals that they are chemically homogeneous. This dichotomy between old and younger Galactic clusters could suggest that they have different mechanisms at the basis of their formation and that the phenomenon of MPs is only possible at high redshifts. In the last few years the idea that MPs phenomenon is only typical of GCs has been challenged by the observation of stars with different N abundance in intermediate-age (ages of $\sim 2-10$ Gyr) star clusters of the Small and Large Magellanic Clouds (SMC and LMC).

Furthermore, in the last dozen years, high-quality CMDs taken with the Advanced Camera for Survey (ACS) and the Wide Field Camera 3 (WFC3) on board the HST disclosed that star clusters younger than ~ 2 Gyr are far from being a single isochrones, revealing the presence of multiple sequences.

1.3.1 Extended Main Sequence Turn-Off

The extended MS Turn-Off (eMSTO) is the most evident feature suggesting that the CMDs of young clusters in the MCs are not representative of single stellar populations. The contingency that this feature could be due to differential reddening or observational errors is usually excluded by the fact that the other CMD sequences, such as the RGB and the AGB, are narrow and well-defined.

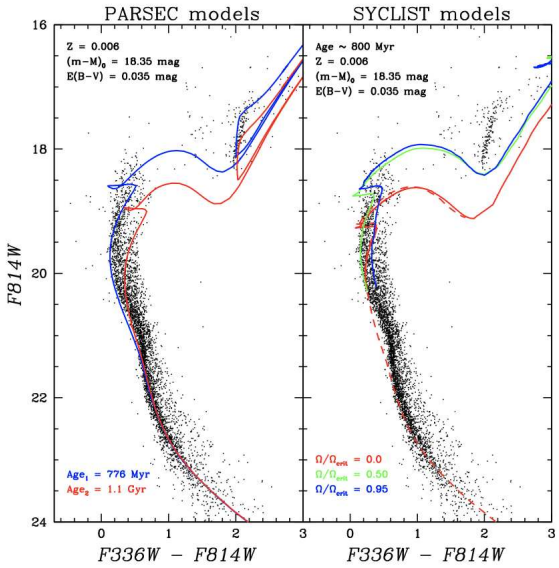

Figure 1.2: Left-hand panel: F814W versus F336W-F814W CMD of NGC 1831 with superimposed best-fitting isochrones from PARSEC for the minimum (blue line) and maximum (red line) age (776 Myr and 1.1 Gyr, respectively) that can be accounted for by the data. Right-hand panel: same CMD as in the left-hand panel, but with superposed isochrones with different rotation rates from the SYCLIST Geneva database. By Correnti et al. (2021).

One interpretation is that eMSTO is due to stars that formed at different times within the parent cluster, with spread in age of $100 - 500$ Myr (Goudfrooij et al. (2014)).

The other main hypothesis is the 'stellar rotation scenario', originally proposed by Bastian and De Mink (2009), where the eMSTO is the result of a spread in rotational velocities among TO stars of a coeval population. According to this idea stellar rotation can imitate the effect of a double or multiple population, whereas in reality only a single population is present. As an example, the analysis by Correnti et al. (2021) of the ~ 800 Myr old star cluster NGC 1831 in the LMC shows (see Figure 1.2) that the morphology of its CMD can be fully explained in the context of the rotation velocity scenario.

This idea will be deeply analyzed in the present work.

1.3.2 Split Main Sequence

Star clusters younger than ~ 800 Myr exhibit a split MS in addition to the eMSTO, with the red MS hosting the majority of MS stars. In all clusters where this feature has been observed, the two MSs merge together for stellar masses smaller than $\sim 1.5 - 1.6$ $M_{\odot}$, which is the mass limit where MS stars would be magnetically braked. Indeed, as proved in the spectroscopic analysis of NGC 1818 by Marino et al. (2018), the most straightforward interpretation of the double MS is the presence of two stellar populations: a sequence of slowly rotating stars lying on the blue-MS (bMS) and a sequence of fast

rotators, with rotation close to the breaking speed, defining a red-MS (rMS).

One example of cluster whose CMD is characterized by a split MS is NGC 1755 a ~ 80 Myr old cluster in the LMC, analyzed by Milone et al. (2016). As shown in Figure 1.3 its CMD shows a split MS with the blue and the red sequences hosting about the 25 per cent and the 75 per cent of the total number of MS stars, respectively. Comparing the observed CMD with isochrones they concluded that observations are not consistent with stellar populations with difference in age, helium, or metallicity only. On the contrary, the split MS is well reproduced by two stellar populations with different rotation. The origin of the split MS could be linked to a braking mechanism (as D'Antona et al. (2017) suggest with tidal braking) that makes fast rotators transition to slow rotators, producing the observed bimodal MS in these young clusters.

Another clear example is NGC 1866, studied by Costa et al. (2019) using a Bayesian method to obtain ages and initial rotation velocities of five well-studied Cepheids of the cluster. As it can be seen in Figure 1.4, the observed multiple main sequences and the turn-offs suggests that the younger ($\sim$ 176 Myr) population is mainly made of slowly rotating stars, while the older ($\sim$ 288 Myr) population is made mainly of initially fast rotating stars, reinforcing the idea that some young clusters like NGC 1866 host multiple populations.

Therefore it is crucial to understand whether the structures observed in the CMDs of star clusters younger than ~ 2 Gyr are entirely due to stellar rotation, or if at least some clusters may host multiple populations.

1.3.3 Double Red Clump

In addition to the eMSTOs and the split MSs, some clusters have shown other distinctive features in their CMDs, including the Dual Red Clump. The Red Clump (RC) is a common feature of the CMDs of intermediate-age clusters gathering stars that are burning He in their cores and are younger and more metal rich with respect to HB stars.

Some clusters exhibit a well-visible secondary clump located below the classical RC. This feature is explained by the scenario in which one of the two groups of stars would avoid e^- degeneracy settling in their H-exhausted cores before He ignites, while the second group would include slightly less massive stars that experience e^- degeneracy before He ignition at the tip of the RGB, thus reaching higher brightness.

One paradigmatic example is NGC 419, an intermediate-age cluster in the SMC that is going to be deeply analyzed in the following chapters. As shown by Girardi et al. (2009), NGC 419 is the rare snapshot of a cluster while undergoing the fast transition from classical to degenerate H-exhausted core.

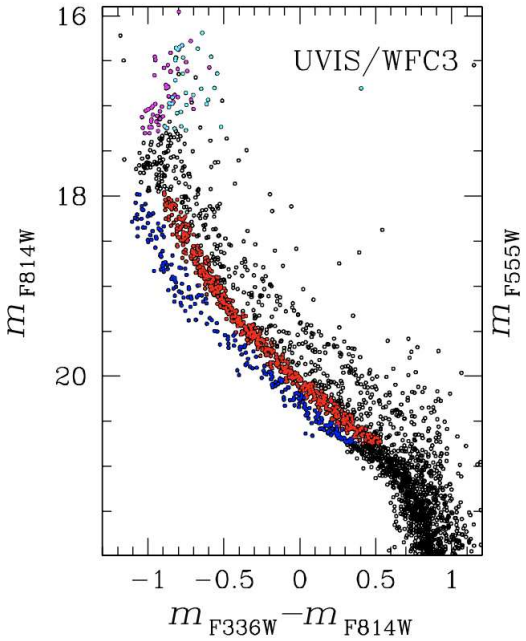

Figure 1.3: CMD of stars in the NGC 1755 field obtained from UVIS/WFC3 photometry. The blue-MS and red-MS stars, selected from UVIS/WFC3 photometry, are coloured red and blue, respectively. By Milone et al. (2016).

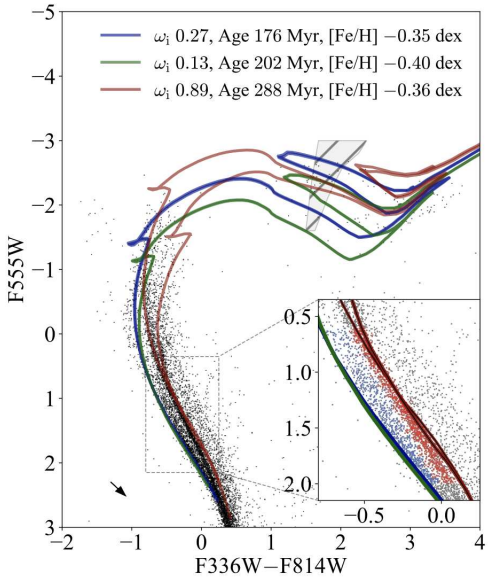

Figure 1.4: Comparison between the NGC 1866 cluster data and selected isochrones in the F555W vs. F336W - F814W CMD. The inclination angles i are 0° (pole on) and 90° (edge on) for the most and less bright isochrones, respectively. By Costa et al. (2019).

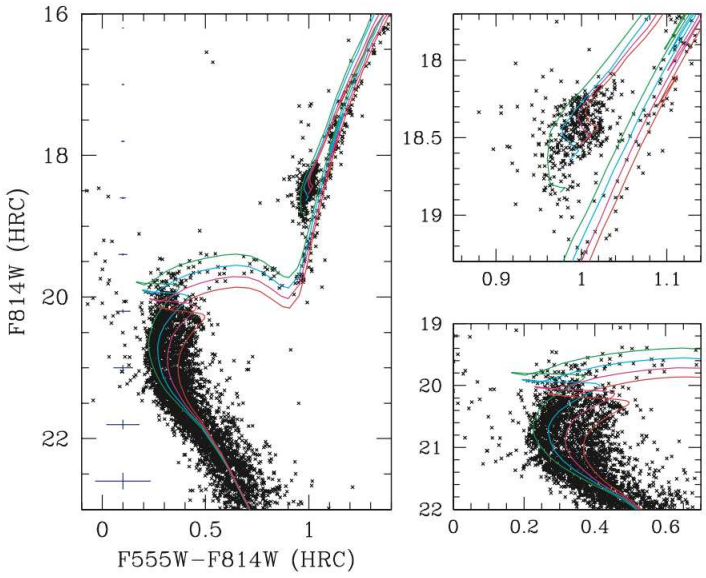

Figure 1.5: The CMD for NGC 419 as derived from the High Resolution Channel data centred on the cluster (left-hand panel). The right-hand panels detail the red clump (top panel) and MSTO regions (bottom panel). The overlaid isochrones are for a metallicity $Z = 0.004$, ages varying from $log(\mathrm{t/yr}) = 9.10$ to 9.25 with a constant spacing of 0.05 dex, $E_{F555W-F814W} = 0.09$ and $(m - M)_{F814W} = 18.85$. By Girardi et al. (2009)

Chapter 2

Stellar rotation and its effect on Colour Magnitude Diagrams

As it was already anticipated in the previous chapter, one of the most surprising recent discoveries in the study of stellar clusters is the fact that they usually show structures in their observed CMDs which cannot be represented by evolutionary isochrones for a single age/metallicity. Of particular interest has been the debate around the origin of bi- or multi- modal distributions in the MSTOs of intermediate age ($1 - 2$ Gyr) clusters in the Magellanic Clouds (MCs).

As previously mentioned, when the distinctive features of the CMDs of these star clusters were discovered, among the first hypotheses proposed to explain their presence was the so-called "age-spread scenario". One of the first works in this regards is the one by Mackey et al. (2008), who aimed to study the reason behind the morphology of the MSTOs of NGC 1846, NGC 1783 and NGC 1806. According to them the simplest explanation is that each cluster is composed of at least two different stellar populations with very similar metal abundances but ages separated by up to $\sim$ 300 Myr. On the other side, although some peculiarities remain unexplained, the "stellar rotation scenario", which attributes these CMD's distinctive features to stellar rotation, is currently gaining more favor compared to the initial hypothesis. This project is guided by these motivations, aiming to also explain features that have not yet been reproduced with rotating models.

2.1 Effects of rotation on stellar structure and evolution

It is clear nowadays that all the stars rotate, as any other object in the universe, and it is a well known evidence since the twentieth century. Studies performed in the last two decades have demonstrated that rotation plays a crucial role in the evolution of stars, affecting every phase of their life. Rotating stars evolve following a different path with respect to the non-rotating ones: typically they are colder and have higher luminosities,

the MS lifetimes are longer, the abundance of elements produced by H-burning on their surfaces is enhanced and they are characterized by bigger cores, leading to different final fates with respect to non-rotating stars.

Historically, the effects of rotation have been examined starting from the work by von Zeipel (1924). In the $60s$ and $70s$ they have been included in polytropic or simplified models, and at the end of the $90s$, more or less extended grids of stellar models that included rotation have appeared.

Rotation modifies the stellar structure and evolution in two main ways (Ekström et al. (2018)):

- With the deformation of the stellar surface: the stellar properties are dependent on the colatitude that is considered, where the colatitude is defined as the distance from the pole. This has an influence on the stellar parameters deduced from observations, and it also induces an anisotropy in the stellar mass loss.
- Some mixing mechanisms are triggered, transporting chemicals and angular momentum, producing a departure from the standard evolution.

2.1.1 Surface deformation

Rotation induces a departure from spherical symmetry that is proportional to the surface rotation rate $\omega_s = \Omega_{\rm surf}/\Omega_{\rm crit}$, where $\Omega_{\rm surf}$ is the rotational velocity at the stellar surface and $\Omega_{\rm crit} = (2/3)^{3/2}\sqrt{8GM/(R_{\rm pol})^3}$ is the critical breakup value, that is the surface velocity at the equator of a rotating star where the centrifugal force balances the Newtonian gravity. Here $R_{\rm pol}$ is the polar value of the stellar radius. Because of the deformation, the effective gravity $\vec{g_{\rm eff}}$ becomes dependent on the rotation rate ω_s and the colatitude θ:

$$\vec{g_{\rm eff}}(\omega_s, \theta) = \left(-\frac{GM}{r^2} + \omega_s^2 r \sin^2\theta\right) \cdot \vec{e_r} + \omega_s^2 r \sin\theta\cos\theta \cdot \vec{e_\theta} \tag{2.1}$$

Contrary to non-rotating stars which are characterized by spherical symmetry, in the case of rotating stars the outcoming flux has to be computed explicitly from integration over the visible surface of the star. Indeed, the flux inherits this dependence form the rotation rate and colatitude:

$$\vec{F}(\omega_s, \theta) = -\frac{L}{4\pi GM^*}\vec{g_{\rm eff}}(\omega_s, \theta) \tag{2.2}$$

This equation is also known as the "Von Zeipel theorem" (von Zeipel (1924)), where M^* is the star effective total mass, that is the mass which would produce the same gravity if there would be no centrifugal force, and L is the luminosity of the star. From this equation it is immediately understandable that the flux emitted by a rotating star depends from both the rotation rate and the inclination angle of the rotation axes of the star with respect to the line of sight.

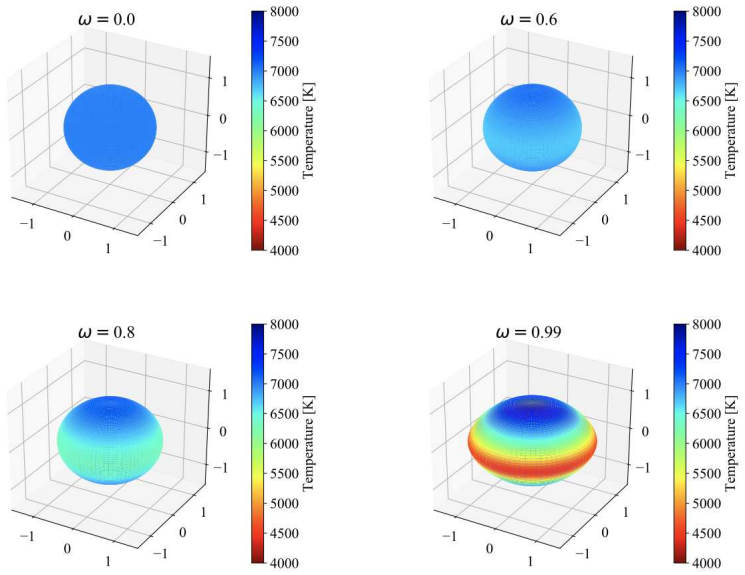

Figure 2.1: Reconstruction of the effective temperature on the star surface for different rotation rates, ω. Different colours represent different effective temperatures. The non-rotating star has $T_{\rm eff} = 7000\,K$. The Von Zeipel theorem was adopted to obtain the effective temperature. By Costa (2019).

Then, according to the Stefan-Boltzman law $\mathrm{F} = \sigma \mathrm{T}^4$, where F is the flux emitted by the blackbody, T is the temperature of the blackbody and $\sigma = 5.66961 \cdot 10^{-5}$ erg cm^{-2} s^{-1} K^{-4} is the Stefan-Boltzmann constant. Assuming that the star emits like a blackbody, this implies that the effective temperature of the star $T_{\rm eff}$ also gets the ω_s - θ dependence:

$$T_{\rm eff} = \left[\frac{L}{4\pi\sigma G M^*} g_{\rm eff}(\omega_s, \theta)\right]^{1/4} \tag{2.3}$$

This equation is valid for slowly rotating stars and describes the gravity darkening effect. Figure 2.1 , that is taken from Costa (2019), clearly shows how rotation affects the effective temperature of a star. A more accurate theoretical description of this effect, that is descriptive also for fast rotating stars, is provided by Espinosa Lara and Rieutord (2011) (equation (31)).

Unless all stellar quantities are specified, equation 2.3 tells how $T_{\rm eff}$ varies across the stellar surface, but not its absolute value. To fix the $T_{\rm eff}$ scale, it could be useful to define the parameter $T_{\rm eff,0}$, which is the $T_{\rm eff}$ that a non-rotating star of the same $R_{\rm pol}$ should have to produce the same luminosity:

$$T_{\rm eff,0} = \left(\frac{1}{4\pi R_{\rm pol}^2} \int_{\rm surface} T_{\rm eff}^4(\theta) dA\right)^{1/4} \tag{2.4}$$

Another important variable is ϵ, defined as the angle between the radial vector and the

normal to the surface. For a 'flattened' rotating star, ϵ is positive for $\theta < 90°$, then rapidly falls to null at the equator, then becomes negative for $90° < \theta < 180°$.

Figure 2.2 shows how the stellar radius, the effective temperature and the surface gravity rescaled to their polar values and the angle ϵ vary with the colatitude for different rotation rates. It can be noticed that the deviations from spherical symmetry are relatively modest for $\omega < 0.5$, but they increase rapidly for higher values of the rotation rate. For example, it is clear from both Figure 2.1 and Figure 2.2 that for fast rotating stars the effect of their rotation is a strong decrease of the $T_{\rm eff}$ in correspondence to the equator. This leads to understand as well the importance of the orientation of a rotating star, indeed if the star deformed by fast rotation is viewed equator-on it will appear dimmer and colder. In this framework we can introduce another fundamental angle i which could be called "viewing angle", but in reality is the "inclination angle" that a rotating star would have as seen on the sky ($i = 0°$ if observed from above the pole, $i = 90°$ when observing from the equator). In addition to that we can also define $F_\lambda^{\rm rot}$, which could be used to compute the flux coming from a rotating star at distance d:

$$F_\lambda^{\rm rot,observed}(i) = \Big(\frac{R_{\rm pol}}{d}\Big)^2 F_\lambda^{\rm rot}(i) \tag{2.5}$$

and such that:

$$F_\lambda^{\rm rot}(i) = \frac{1}{R_{\rm pol}^2}\int_0^{2\pi}\int_0^{\pi} I_\lambda(\mu')\mu'(r^2/\cos\epsilon)\sin\theta d\theta d\phi \tag{2.6}$$

In this expression, compared to the spherical case, the infinitesimal element of surface area has two new multiplicative factors: r^2 taking into account the increase of the area due to the dependence of r with θ, and $(1/\cos\epsilon)$ taking into account the increase of the area because of the inclination of the surface elements with respect to the radial direction. Here μ' is the cosine of the angle between the normal to the stellar surface and the direction of the observer. Several $F_\lambda^{rot}(i)$ are shown in the left-hand panel of Figure 2.3. It is quite clear that if the star is viewed pole-on it will be much brighter and bluer, than when seen equator-on.

Given the equations for $F_\lambda^{rot}(i)$ it is possible to derive bolometric corrections BC_{S_λ} as it is done in Section 2.5 of Girardi et al. (2019), which make it possible to transform the bolometric magnitudes into absolute magnitudes as a function of i, $M_{S_\lambda} = M_{bol} - BC_{S_\lambda}$, for any filter transmission curve S_λ. Actually, a large amount of tabulations of the BCs for non-rotating stars, as a function of $T_{\rm eff}$, $log(g)$, and $[Fe/H]$, are already available. Therefore, it may be convenient to work with the 'changes in BC caused by the rotation', rather than with the absolute BCs themselves:

$$\Delta BC_{S_\lambda}(i,\omega,T_{\rm eff,0},log\,g_{\rm pol}) = 2.5\;log\Big(\frac{\int_{\lambda_1}^{\lambda_2}\lambda F_\lambda^{\rm rot}(i,\omega,T_{\rm eff,0})S_\lambda d\lambda}{\int_{\lambda_1}^{\lambda_2}\lambda F_\lambda^{\rm rot}(T_{\rm eff,0},log\,g_{\rm pol})S_\lambda d\lambda}\Big) \tag{2.7}$$

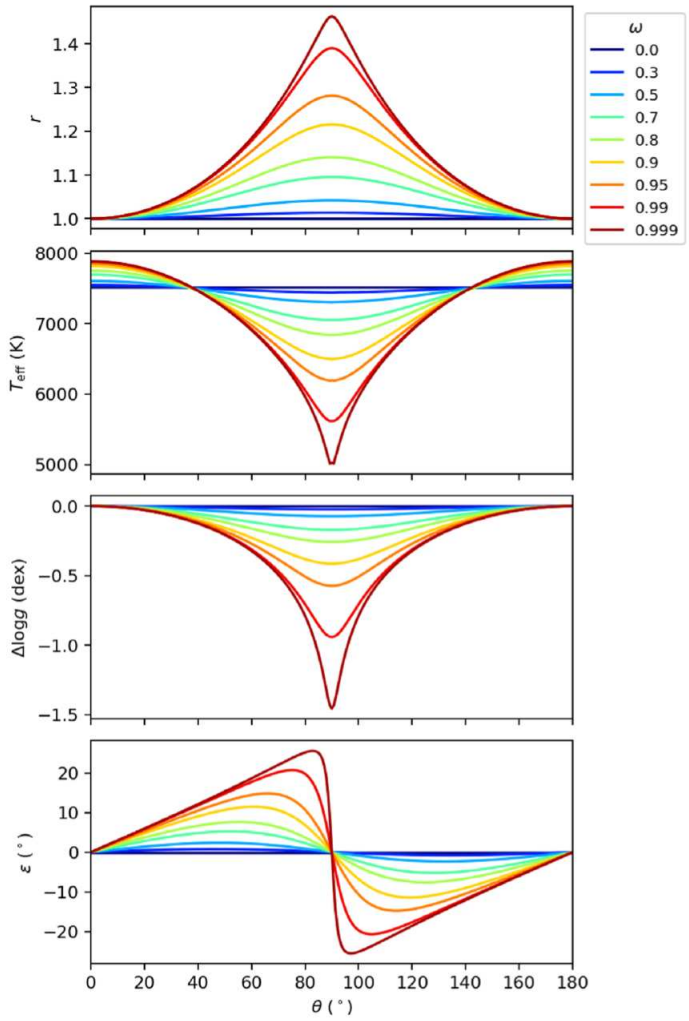

Figure 2.2: Variation of stellar surface quantities with the angle θ, for stars with $T_{\rm eff,0} = 7500\ K$ and several values of ω. Panels from top to bottom show the stellar radius rescaled to its polar value r, the local effective temperature and the surface gravity with respect to its polar value, and the angle ϵ. By Girardi et al. (2019).

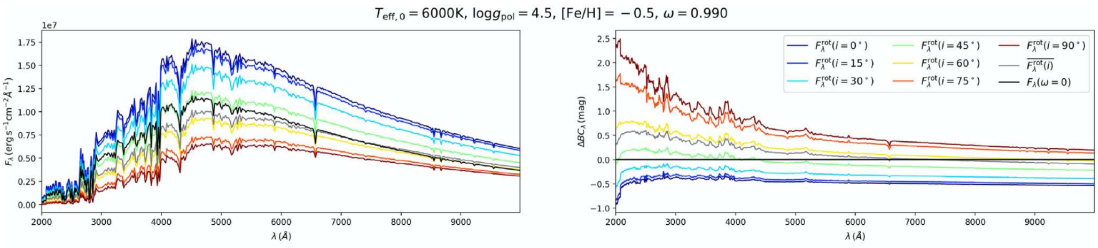

Figure 2.3: Left-hand panel: $F_\lambda^{\rm rot}(i)$ computed for a star of $T_{\rm eff,0} = 6000$ K, and for a fixed $\omega = 0.99$, $\log g_P$, and $[Fe/H] = -0.5$ dex. Coloured lines show the $F_\lambda^{\rm rot}$ observed from various angles from the pole ($i = 0°$, bluer) to the equator ($i = 90°$, redder). The gray line is the mean F_λ averaged from all possible lines of sight, $F_\lambda^{\rm rot}(i)$. Finally, the dark line is the F_λ computed for the non-rotating star of same $T_{\rm eff,0}$. Right-hand panel: the same models but now plotting, in a magnitude scale, the relative flux of the rotating models compared to the reference non-rotating star – i.e. plotting $\Delta BC_\lambda = -2.5 \log[F_\lambda(\omega = 0.99)/F_\lambda(\omega = 0)]$. By Girardi et al. (2019).

In this way, the $\Delta BC_{S_\lambda}(i, \omega, T_{\rm eff,0}, log\, g_{\rm pol})$ computed for limited grids can be used for a wide variety of rotating stars. A set of ΔBC_{S_λ} tables are inserted in the TRILEGAL code, that is used in the present work for the production of isochrones.

2.1.2 Mixing mechanisms

Usually, in non rotating stellar models the mixing process takes place only in regions of the star that are in the convective regime while in the radiative zones elements are not subject to mixing. Opposite to this case, in rotating stars, the elements mixing takes place also in the radiative regions of the stars. Other than the distortion of the stellar structure, rotation produces instabilities that bring to a redistribution of the chemical elements and of the angular momentum throughout the star. Depending on the value of the rotation rate, the extra-mixing provided by rotation could affect the evolution of the star in a non-negligible way. As described by Costa (2019), the two main causes of extra mixing are:

- The meridional circulation, also known as the Eddington-Sweet circulation, is a macro motion of the stellar material from poles to the equator or the reverse, due to the thermal imbalance of a rotating star;
- The shear instability, due to the different rotation velocity of two nearby shells of the star, drives to turbulent mixing of the chemical elements between the layers.

The two cited instabilities actually have a sort of hierarchical dependence, in fact, consequently to the geometric distortion of the star due to rotation, meridional circulation takes place, which in turn produces the differential rotation leading to shear instabilities.

The net effect of rotational mixing is to recharge the core with new fuel, leading to the formation of larger cores, extending the lifetime of the star, and the increase of the luminosity. Actually, the behaviour of a star is not monotonic for increasing ω. On the

other side, at the beginning of the MS, the hydrostatic effects dominate and the star behaves like a lower-mass one. As evolution goes on, the mixing becomes dominant for low and average rotation, while the rapid rotators keep strong hydrostatic effects. The highest L is therefore observed not in the fastest stars, but in slightly-above-average rotators.

2.2 Effects on the CMD

Regarding the effect of stellar rotation on the CMDs of stellar populations, it was only recently recognized that it could be playing a very important role in determining the photometric properties of stars born in populous star clusters in the MC and MW open clusters. For example, spectroscopic observations have identified fast rotators in NGC 1866 and NGC 1818, clusters in the LMC. These clusters have often been used to calibrate non-rotating stellar models, so ignoring rotation may have had significant consequences. This oversight could have led to systematic errors in age estimates of well-studied clusters and an overestimation of the amount of convective core overshooting needed to replicate the luminosity of post-main-sequence stars. Therefore, it is crucial to include rotation in previous sets of stellar models to study such clusters and the multitude of field stars that likely began their nuclear-burning lives as fast rotators.

As already said in the previous section, the reduced gravity in rotating stars results in lower luminosities and effective temperatures. Also the orientation of the star with respect to the line of sight is important: a star deformed by fast rotation appears brighter and hotter if viewed pole-on. These effects can significantly alter the colour and magnitude of stars, and therefore the CMD of a cluster. In addition, mixing processes induced by rotation modify the composition of the stellar envelope and effectively increase the size of the stellar core, resulting in higher luminosities and cooler temperatures for turn-off stars.

In order to better illustrate the effects of rotation on the CMD, especially in the region of the eMSTO, isochrones corresponding to different rotation rates are superimposed on the data of the NGC 419 star cluster of the SMC in Figure 2.4. This is done for the two extreme values of inclinations, $i = 0°$ in the left-hand panel and $i = 90°$ in the right-hand panel, to show the effects of different inclination angles as well. The NGC 419 data were taken with the HST Wide Field Channel (WFC) of the ACS selecting an area of $\sim$ 1257 arcsec^2. The overplotted isochrones are produced by the TRILEGAL code (Girardi et al. (2005a)) starting from the set of evolutionary tracks computed by PARSEC V2.0 code (Nguyen et al. (2022)) accounting for stellar rotation (see 4.1 for more details). At the level of the TO, when $i = 0°$ (pole-on configuration), isochrones with high rotation rate have higher luminosity with respect to ischrones with lower $\omega_{\rm i}$, as expected due to both the mixing processes and the deformation induced by rotation. On the other side, when $i = 90°$, as expected in accordance with the findings represented in Figure 2.1, isochrones corresponding to fast rotation show much cooler temperatures with respect to isochrones with lower $\omega_{\rm i}$. Moreover, it is worth noticing that, in the

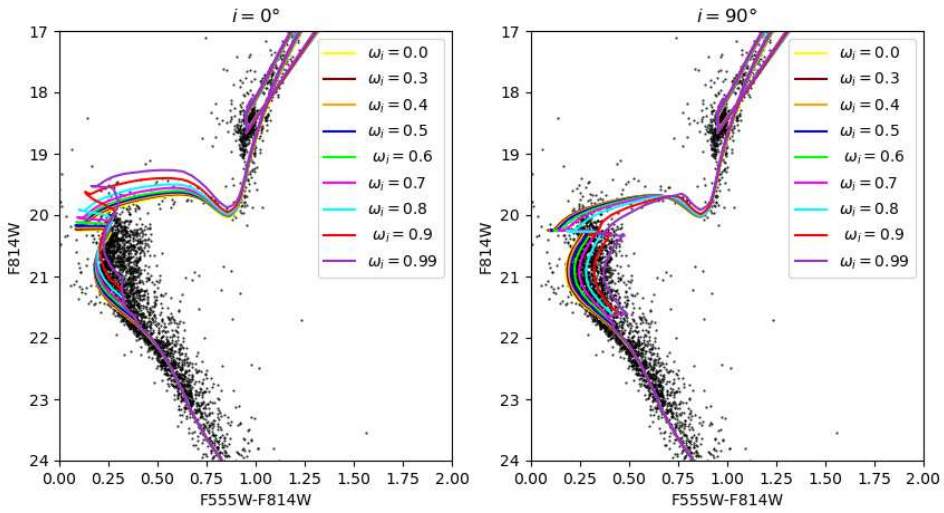

Figure 2.4: Left: the CMD for NGC 419 as derived from the ACS data centered on the cluster. The overlaid isochrones are for a metallicity $Z = 0.004$, age $log(\mathrm{t/yr}) = 9.125$, inclination $i = 0°$, distance modulus $(m - M)_0 = 18.89$, absorption in V band $A_\mathrm{v} = 0.15$ and rotation rate from $\omega_\mathrm{i} = 0.0, 0.1, 0.3, 0.2, 0.4, 0.5, 0.6, 0.7, 0.8, 0.9, 0.99$. Right: the same as the left-hand panel but with inclination $i = 90°$.

case in which $i = 90°$, the evident spread of the MSTO could be easily reproduced with isochrones corresponding to stellar populations with the same age but different initial rotation rate ω_i.

As already anticipated at the end of section 2.1.1, apart from rotation, the inclination angle plays a crucial role in affecting the position of single stars in the CMD. In particular, if the rotating star is viewed pole-on ($i = 0°$) it will be much brighter and bluer, than when seen equator-on ($i = 90°$). This effect is the responsible for the position of the isochrones in Figure 2.5. Dashed isochrones and solid-line isochrones are perfectly superimposed in all evolutionary phases except for the MSTO region. It is worth noticing that here the solid and dashed isochrones are almost superimposed for $\omega_\mathrm{i} = 0.5$, while there is a noticeable difference in brightness and colour (the isochrones with $i = 0°$ is bluer and brighter with respect to the corresponding dashed isochrone with $i = 90°$) shown by highly rotating stars ($\omega_\mathrm{i} = 0.99$), enlightening that the effect of gravity darkening depends on the amount of rotation rate. This suggests that if stars in a cluster do not have a preferred angle of inclinations, but a distribution of various inclination, high rotating stars could populate such region of the HR diagram creating the eMSTO.

2.2.1 Magnetic breaking and disappearance of the eMSTO

If the "stellar rotation scenario" is correct, it is expected that the eMSTO phenomenon disappears for clusters that are old enough. This is explained by the fact that below

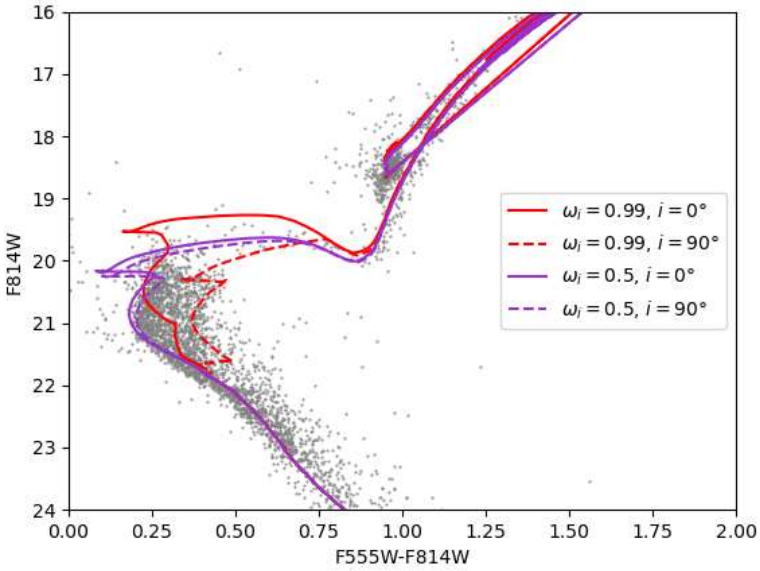

Figure 2.5: The CMD for NGC 419 as derived from the ACS data centered on the cluster. The overlaid isochrones are for a metallicity $Z = 0.004$, age $log(\mathrm{t/yr}) = 9.125$, distance modulus $(m - M)_0 = 18.89$, absorption in V band $A_\mathrm{v} = 0.15$. Red isochrones correspond to a rotation rate $\omega_\mathrm{i} = 0.99$, while purple isochrones correspond to $\omega_\mathrm{i} = 0.5$. Solid lines indicate isochrones with $i = 0°$ while dashed lines indicate isochrones with $i = 90°$

a given mass stars undergo magnetic braking early on the MS, making their tracks converge towards those of non rotating stars. This braking is caused by the interaction of stellar winds with the surface magnetic field that is produced by a dynamo process in the external convective envelope of the star. When the convective envelope becomes thick enough magnetic braking efficiently spins down the star, hence suppressing both the stellar deformation and chemical mixing effects. It follows that when these stars are at the level of the MSTO, their slowed rotation causes the disappearance of the eMSTO phenomenon. Georgy et al. (2019) investigated the occurrence of this phenomenon at different metallicities, determining the age above which no eMSTO is expected in the CMDs of stellar clusters. Their models show that the age at which the eMSTO disappears increases with increasing metallicity, being ~ 2 Gyr at the LMC metallicity. Highlighting the presence of this phenomenon is crucial as it reinforces the significance of stellar rotation as a key factor in causing the eMSTO in young and intermediate age clusters.

Chapter 3

Target Clusters

The Magellanic Clouds (MCs), two irregular dwarf galaxies that orbit the MW, have long been of great interest to astronomers. They are located close enough to us that their stars can be resolved individually, making them ideal targets for studying stellar populations and their properties. One of the most interesting aspects of the MCs is their rich population of open clusters, particularly many of these clusters are much more rich in stars than clusters of similar age in the MW. Open clusters offer a unique window into the early stages of star formation and evolution, providing valuable insights into the processes that shape the properties of stars and their environments.

In recent years, it has become increasingly accepted that the open clusters in the MCs harbor stars with a significant spread in rotational velocity. It follows that these objects are particularly well-suited for studying and understanding the distribution of rotational velocities of their stars. For this reason four clusters belonging to these environments were chosen for this work, NGC 419 in the SMC and NGC 2203, NGC 1831 and NGC 1866 in the LMC. All these clusters are very rich in stars, and present all the interesting features associated with rotation in their CMDs.

The upcoming sections of this chapter will feature a brief introduction to each of the studied clusters, while the main parameters derived from literature (Goudfrooij et al. (2014) for NGC 419 and NGC 2203; Correnti et al. (2021) for NGC1831; Gossage et al. (2019) and Goudfrooij et al. (2018) for NGC 1866) are listed in Table 3.1.

3.1 NGC 419

NGC 419 is an intermediate-age ($t = 1.45 \pm 0.05$ Gyr, see Goudfrooij et al. (2014)) star cluster located to the east of the SMC's bar in a region relatively devoid of dust. Its celestial coordinates for the J2000 equinox are $\alpha\,(RA) = 01^h08^m17.2^s$ and $\delta\,(DEC) = -72°53'01''$ (from SIMBAD database). It was discovered on September 2, 1826 by James Dunlop and it was described by Dreyer as "pretty large, pretty bright, round, gradually

Table 3.1: Main parameters of our target clusters. Row 1: age in gigayears. Row 2: metallicity in dex. Row 3: distance modulus. Row 4: V-band foreground extinction. These values are taken from literature: [1]:Goudfrooij et al. (2014), [2]:Correnti et al. (2021) [3]:Goudfrooij et al. (2018) [4]:Gossage et al. (2019)

Parameter	**NGC 419**	**NGC 2203**	**NGC 1831**	**NGC 1866**
Age (1)	$1.45 \pm 0.05^{[1]}$	$1.55 \pm 0.05^{[1]}$	$\sim 0.8^{[2]}$	$\sim 0.25^{[3]}$
$[Fe/H]$ (2)	$-0.7 \pm 0.1^{[1]}$	$-0.3 \pm 0.1^{[1]}$	$-0.25^{[3]}$	$-0.36^{[4]}$
$(m-M)_0$ (3)	$18.85 \pm 0.03^{[1]}$	$18.37 \pm 0.03^{[1]}$	$18.35^{[2]}$	$18.43^{[3]}$
$A_{\rm v}$ (4)	$0.15 \pm 0.02^{[1]}$	$0.16 \pm 0.02^{[1]}$	$0.11^{[2]}$	$0.28^{[3]}$

brighter middle."

Figure 3.1: NGC 419 based on observations made with the NASA/ESA Hubble Space Telescope, and obtained from the Hubble Legacy Archive.

NGC 419 is one of the greatest examples of star clusters with a composite structure of main and secondary RC. The presence of a secondary clump in this cluster was indeed noted by Glatt et al. (2008), who have suggested it to be 'a red clump of the old SMC field star population'.

On the other side, as already anticipated in Section 1.3.3, according to the analysis performed by Girardi et al. (2009) NGC 419 is the rare snapshot of a cluster while undergoing the fast transition from classical to degenerate H-exhausted core. In particular, they use synthetic CMDs to show that the double RC feature corresponds very well to the secondary clump which is predicted to occur due to He-ignition in stars that are just large enough to avoid e^--degeneracy in their H-exhausted cores. In contrast, the primary RC is composed of stars that are slightly less massive and have gone through e^--degeneracy, subsequently igniting He at the top of the RGB.

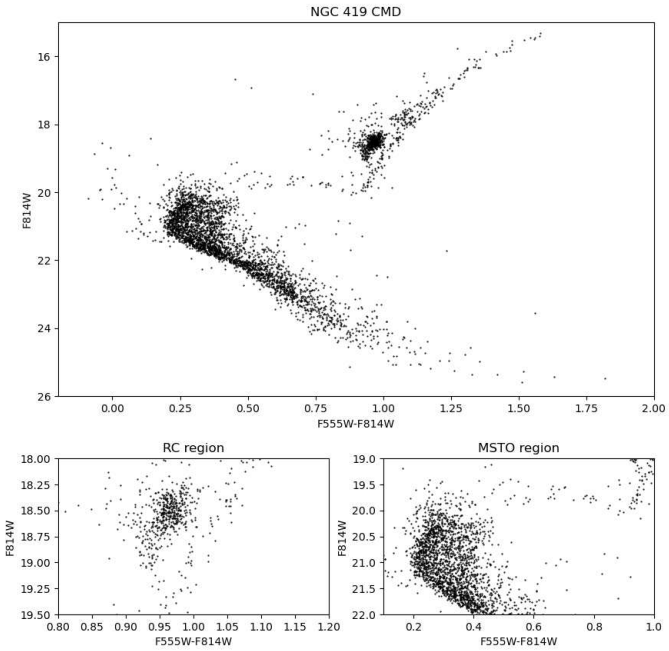

Figure 3.2: Top panel: The colour-magnitude diagram for NGC 419 as derived from HST observation. Bottom panels: details of the RC (left) and MSTO (right) regions.

The NGC 419 data were taken with the WFC of the ACS on board the HST selecting an area of $\sim 1257\ arcsec^2$. The observations were performed in the F555W and F814W filters. The CMD of the observations in Figure 3.2 reveals a distinct double RC, which is especially noticeable in the lower-left panel. Additionally, the presence of an evident eMSTO is noteworthy. These features suggest that NGC 419 is a suitable cluster for this work wherein we aim to simulate the properties of the observed CMD employing rotating evolutionary models, that encompass all evolutionary phases (including the RC).

3.2 NGC 2203

NGC 2203 is the oldest object among our target clusters. It is an intermediate-age ($t = 1.55 \pm 0.05$ Gyr, as derived by Goudfrooij et al. (2014)) open cluster located in the southern constellation of Mensa. Also known as $ESO\ 34-4$ and $LW380$, it was discovered by the English astronomer John Herschel on January 23, 1836. This cluster is a distant outlyer of the LMC and it is approximately 31 light-years across. Its celestial coordinates for the J2000 equinox are $\alpha\,(RA) = 06^h04^m42.0^s$ and $\delta\,(DEC) = -75°26'18''$ (from SIMBAD database).

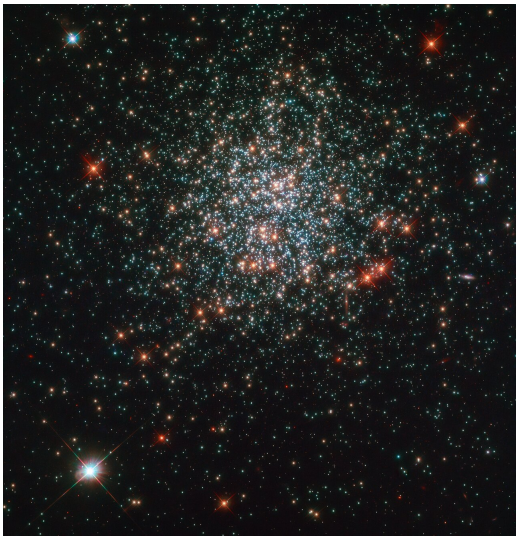

Figure 3.3: NGC 2203 based on observations made with the NASA/ESA Hubble Space Telescope.

The cluster's CMD was obtained from the HST WFC of the ACS and the data set consists of a $\sim 5026\ arcsec^2$ area . The observations were conducted using F475W and F814W filters. The CMD shows a clear eMSTO, but unlike NGC419, the secondary RC appears to be quite faint. These properties can be seen in Figure 3.4.

Gossage et al. (2019) studied this cluster, trying to assess the statistical effectiveness of three proposed scenarios in explaining the eMSTO morphology in different star clusters: (1) an extended star formation, (2) a rotation-rate distribution, and (3) a combination of both. NGC 2203, which is the older cluster of the study, is among the worst-fit clusters, together with NGC 1866. These two are the only cases where an age spread appears to significantly outperform the pure rotation model. On the other side, Gossage et al. (2019) finds it plausible that a Gaussian age spread could potentially account for missing aspects, possibly the phenomenon of magnetic breaking (see 2.2.1) in this case. In this work we will try to model the CMD of NGC 2203 by assuming a pure rotation scenario.

3.3 NGC 1831

NGC 1831 is a $\sim$ 800 Myr old open cluster of the LMC, located in the constellation of Dorado. It was discovered by the Scottish astronomer James Dunlop in 1826. Its celestial coordinates for the J2000 equinox are $\alpha\,(RA) = 05^h06^m16.7^s$ and $\delta\,(DEC) = -64°55'03''$ (from SIMBAD database).

Observations of the cluster NGC 1831 were obtained using the Ultraviolet and Visual Channel of the Wide Field Camera 3 (UVIS/WFC3) of HST. The observations were conducted using two filters, namely F336W and F814W and the data set consists of a circular area, centered on the cluster, with radius $\sim$ 35.2 arcsec. Selecting the F336W

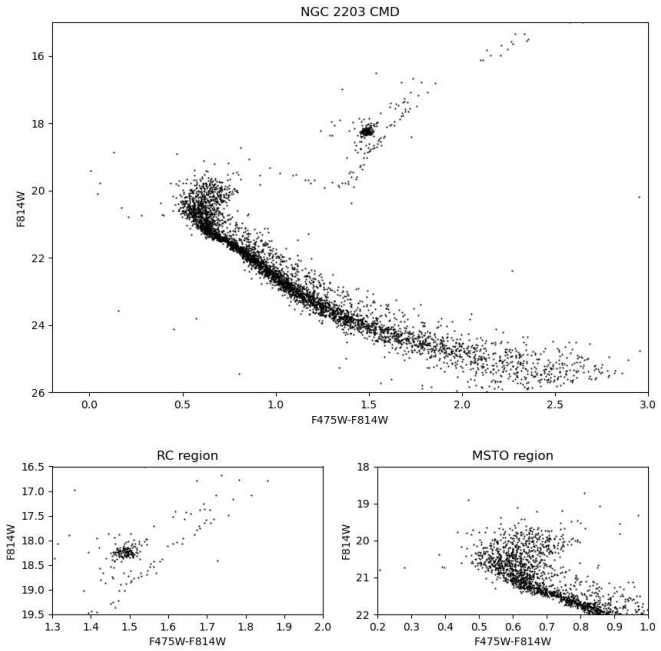

Figure 3.4: Top panel: The colour-magnitude diagram for NGC 2203 as derived from HST observation. Bottom panels: details of the RC (left) and MSTO (right) regions.

as the blue filter offers a balanced approach by providing a reasonable exposure time while still allowing the detection of noticeable colour differences between stars exhibiting different rotation rates. The relative CMD is plotted in Figure 3.6. This plot clearly shows the presence of an eMSTO and a quite extended RC.

Moreover, the CMD can be divided in two parts, above and below the kink at $F814W \sim 21\,mag$. Each part is characterized by a different morphology. Above this limit, the MS and MSTO are more broadened than what is expected from a SSP, while below the kink, the shape of the MS reminds a SSP. According to Goudfrooij et al. (2018), both the shape and location of this feature, together with the fact that it is not well described by isochrones, suggests that its nature is linked to the sudden onset of strong convection in the outer layers of stars. Indeed, as shown by D'Antona et al. (2002), this kink occurs at a stellar mass for which the convective envelope suddenly reaches much deeper into the interior than it does at a mass only $0.01 M_{\odot}$ larger, thus causing a significant decrease of the temperature dependence of stellar mass, $dT_{\rm eff}/dM$, with decreasing stellar mass. Since the $T_{\rm eff}$ at the MS kink is $\sim$ 7800 K, for which the stellar continuum peaks at $\sim$ 3700 $\mathring{A}$ according to Wien's law, this sudden decrease of $dT_{\rm eff}/dM$ is measured most precisely using filters around that wavelength with a

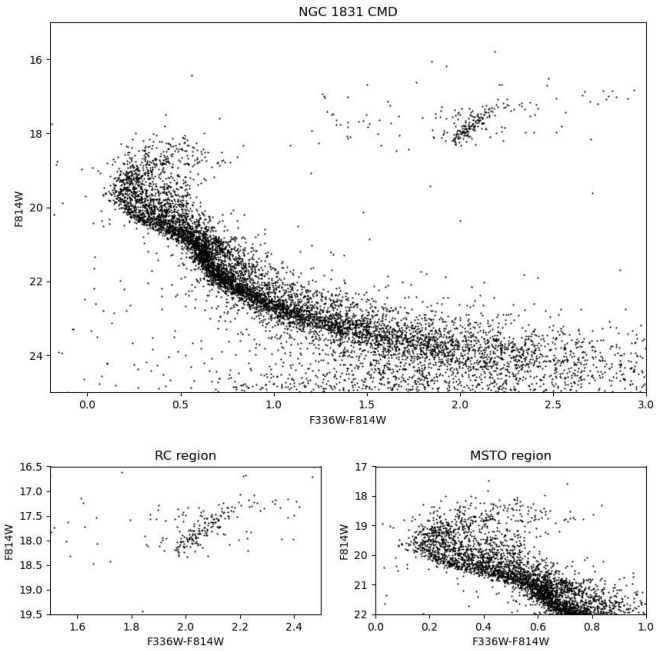

Figure 3.5: Top panel: The colour-magnitude diagram for NGC 1831 as derived from HST observation. Bottom panels: details of the RC (left) and MSTO (right) regions.

wide baseline, such as $F336W - F814W$. Goudfrooij et al. (2018) states that the MS kink seen in NGC 1831 and the younger LMC clusters is associated with this sudden change in the extent of the convective envelope at the metallicity of the young and intermediate-age LMC clusters. Furthermore, since the width of the single-star MS emerging down from the MS kink in NGC 1831 is fully consistent with an SSP, this suggests that the kink also represents an empirical measure of the stellar mass below which rotation has no appreciable influence on the energy output of the star. It is worth to mention that the feature of the MS kink is included in the computation of PARSEC isochrones. Particularly, it is widely acknowledged that low-mass stars generally do not attain high rotational speeds, unlike intermediate and high-mass stars. In cases where convection is well developed, rotation may initially achieve high values for certain masses. For this reason, as described Nguyen et al. (2022), similar to how convective overshooting efficiency is considered, rotation was not taken into account for stars with masses $M_i \leq M_{\rm O1}$. However, for stars with masses $M_i \geq M_{\rm O2}$, models were calculated with various initial rotation rates: $\omega_{\rm i} = 0.0, 0.30, 0.60, 0.80, 0.90, 0.95, 0.99$. For stars whose initial mass lies in the range $M_{\rm O1} \leq M_i < M_{\rm O2}$, rotation is gradually introduced

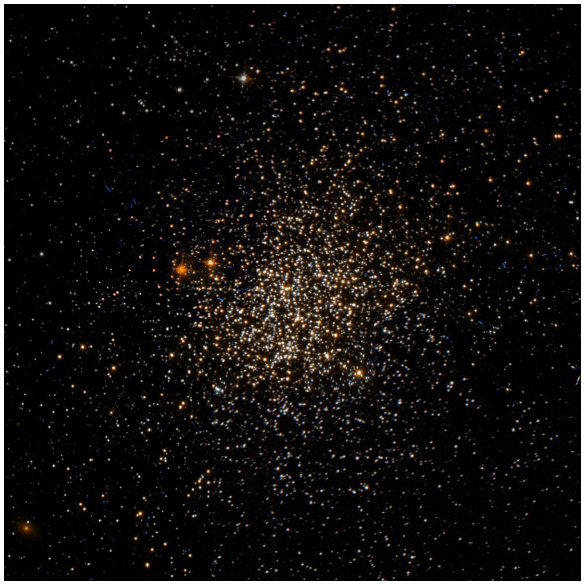

Figure 3.6: NGC 1831 based on observations made with the NASA/ESA Hubble Space Telescope, and obtained from the Hubble Legacy Archive.

and models are computed with an initial rotation rate up to a maximum value of:

$$\omega_{\mathrm{i,max}}(M) \equiv 0.99\Big(\frac{M - M_{\mathrm{O1}}}{M_{\mathrm{O2}} - M_{\mathrm{O1}}}\Big) \tag{3.1}$$

where M_{O1} is the largest initial mass of a star showing a vanishing convective core during the early hydrogen burning phase, and $M_{\mathrm{O2}} = M_{\mathrm{O1}} + 0.3$ is the mass above which the overshoot is applied with its maximum efficiency and rotation is fully considered. Hence, given that the MS kink represents an empirical measure of the stellar mass above which rotation sets in, this approach by Nguyen et al. (2022) also describes how the feature of the MS kink is artificially introduced in PARSEC isochrones. In Figure 3.7 TRILEGAL isochrones obtained from PARSEC stellar tracks are plotted on top of NGC 1831 data, for the two extreme values of the initial rotation rate $\omega_{\mathrm{i}} = 0.0$ and $\omega_{\mathrm{i}} = 0.99$ and a value of the inclination angle of $i = 90°$ for both cases. It is worth to notice how the MS kink feature is completely absent in the non-rotating isochrone, while it is present at $F814W \sim 21\,mag$ in the isochrone with $\omega_{\mathrm{i}} = 0.99$. At this point, for all the reasons said above, it is possible to get an estimate of the initial mass at which rotation sets in (M_{rot}) by looking at the maximum mass for which the non-rotating isochrone stays on top of the data. For NGC 1831 this happens at $F814W \sim 21.4\,mag$ and $M_{\mathrm{rot}} \sim 1.35 - 1.4\ M_{\odot}$.

Furthermore, this cluster was deeply analyzed in Correnti et al. (2021). To examine whether a specific scenario (age spread versus stellar rotation) can accurately replicate the observed CMD, they compared the cluster's CMD morphology with Monte Carlo simulations. These simulations involved synthetic star clusters consisting of multiple SSP of different ages, or single SSP with a range of rotation velocities. The results

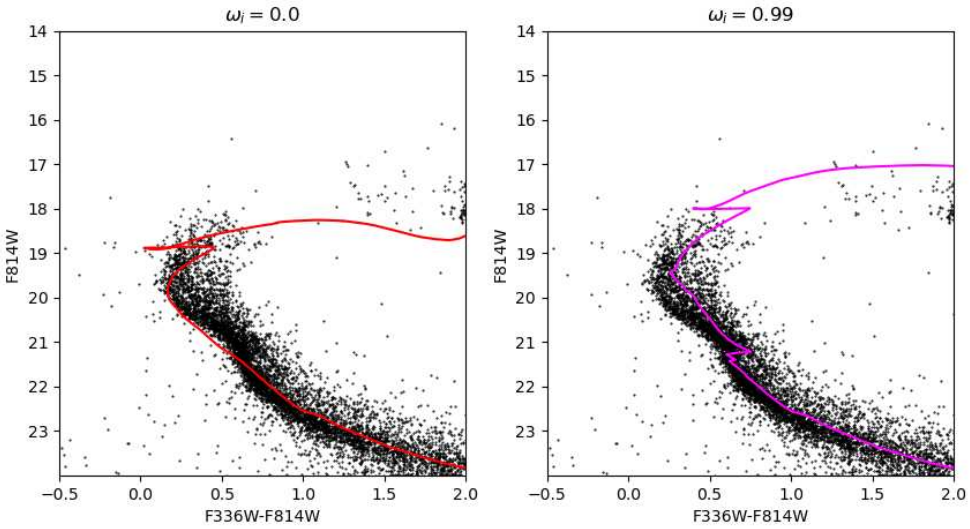

Figure 3.7: The colour-magnitude diagram for NGC 1831 as derived from HST observation with overplotted isochrones obtained with TRILEGAL for two values of the initial rotation rate $\omega_{\rm i} = 0.0$ (left-hand panel) and $\omega_{\rm i} = 0.99$ (right-hand panel). The value of the inclination angle for the rotating isochrone is $i = 90^{\circ}$

indicate that while the simulation based on the age spread scenario provided a very good fit for the extended main sequence turnoff (eMSTO), it failed to reproduce the full colour width of the main sequence (MS). In contrast, the morphology of NGC 1831 can be fully explained within the context of the rotation velocity scenario, under the assumption of a bimodal distribution for the rotating stars, with $\sim 40\%$ of stars being slow rotators and the remaining $\sim 60\%$ being fast rotators. It will be interesting to determine whether our findings align with the outcomes of this study.

3.4 NGC 1866

NGC 1866, with an age of approximately 250 Myr, is the youngest cluster of this study and it is located in the LMC, in the constellation of Dorado. As NGC 1831, this cluster was discovered in 1826 by James Dunlop. Located at the northern periphery of the LMC disc, it remains relatively unaffected by interstellar dust and field stars. Due to this unique location, it becomes a captivating choice for examining intermediate-age stellar populations. Its celestial coordinates for the J2000 equinox are $\alpha\,(RA) = 05^h13^m38.9^s$ and $\delta\,(DEC) = -65^{\circ}27'52.75''$ (from SIMBAD database).

The NGC 1866 photometric data were acquired through the UVIS-WFC3 on board the HST. The cluster was observed in the two pass-band filters F336W and F814W. Data were selected within a circular region of approximately 35.0 arcsec in radius. Figure 3.8 shows the F814W vs. F336W - F814W CMD of this cluster. The choice of a wide

wavelength baseline is driven by the fact that as colour stretches out it enhances our ability to discern the split-MS and the eMSTO.

As anticipated in Section 1.2, this cluster was investigated by Costa et al. (2019) by analyzing a sample of five Cepheids of the cluster with a Bayesian statistical method. Moreover, they fitted the cluster features (the MS split and the eMSTO) with new PARSEC isochrones incorporating overshooting and rotation. This research revealed interesting findings about the five Cepheids in the cluster. Four of the Cepheids were identified as belonging to a younger population with initially slow rotation, estimated to be approximately 176 ± 5 million years old. On the other side, the fifth Cepheid showed a greater age, presenting two possible scenarios: around 288 ± 20 Myr if it had a high initial rotational velocity ($\omega_{\rm i} \sim 0.9$), or approximately 202 ± 5 Myr for models with slower initial rotation. However, the additional analysis of the CMD effectively ruled out the latter option and instead provided strong evidence for the existence of two distinct populations in the cluster, approximately 176 Myr and around 288 Myr old, respectively. Hence, it seems that this work einforces the idea that some young clusters like NGC 1866 may host multiple populations.

Another study related to this cluster is the one performed by Gossage et al. (2019), who tried to infer which scenario among the three proposed ones (an extended star formation, a rotation-rate distribution, and a combination of both) provides the best-fit of its CMD. Through their analysis of NGC 1866, they discovered that the pure rotation rate model has a tendency to exhibit discrepancies within the observed eMSTO region. On the other side a Gaussian age spread may optimize the fit in this case. This result seems to be consistent with the presence of an age spread within the stars of this cluster, as also suggested by Costa et al. (2019). However, Gossage et al. (2019) also proposes the possibility that the Gaussian age spread might be compensating the absence of certain aspects, such as the omission of modeling the decretion disks of Be stars, whose presence is plausible in NGC 1866. Therefore, it might be interesting to include this cluster in the present work and see if fitting the CMD with PARSEC rotating stellar models can let us explain its morphology.

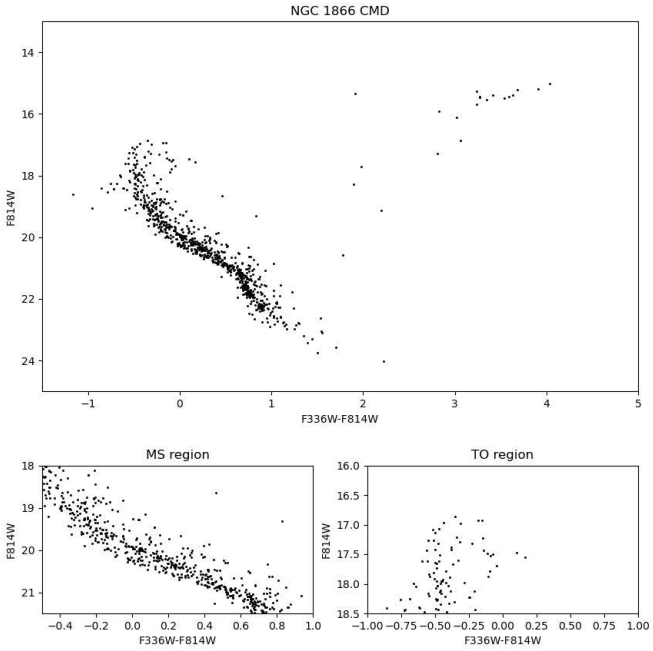

Figure 3.8: Top panel: The colour-magnitude diagram for NGC 1866 as derived from HST observation. Bottom panels: details of the split MS (left) and MSTO (right) regions.

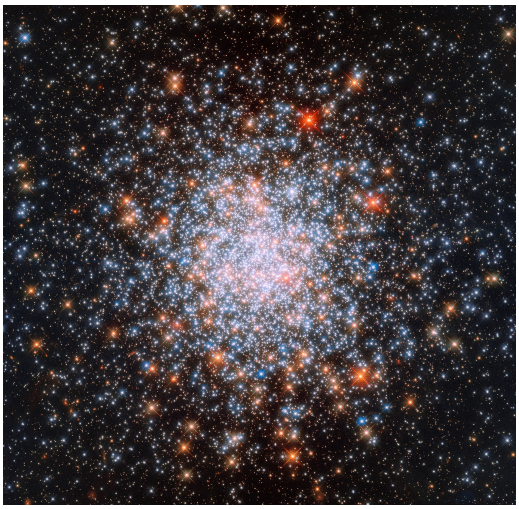

Figure 3.9: NGC 1866 based on observations made with the NASA/ESA Hubble Space Telescope, and obtained from the Hubble Legacy Archive.

Chapter 4

Analysis methodology

The purpose of this study is to investigate the rotational velocity distribution of stars in the star clusters of the MCs introduced in Chapter 3. To achieve this, the general approach is to generate stellar populations, each with a different rotation rate, based on the isochrones obtained from PARSEC V2.0 stellar tracks (Nguyen et al. (2022)). These stellar populations are referred to as "Partial Models" (PMs), and they are generated in form of Hess diagrams, which are matrix representations of the stellar density across the CMD. Once the PMs are obtained they are fed to *sfhfinder* code (Mazzi et al. (2021)) to derive both the best-fitting solution that better represents the observed data and the confidence intervals of the fitted parameters. In particular, the final model is a linear combination of the PMs, telling us the relative importance of each population corresponding to each rotational velocity. This procedure is performed for different age and metallicity bins, chosen accordingly to which cluster is being analyzed.

4.1 PARSEC V2.0 isochrones

The PAdova and tRieste Stellar Evolutionary Code (PARSEC) was first implemented in Bressan et al. (2012) and then used in several works aimed at producing large grids of stellar tracks and isochrones. More recently, Costa et al. (2019) made further advancements to the code by incorporating the influence of rotation, resulting in the updated version, PARSEC V2.0 (Nguyen et al. (2022)). The major differences between the last version and the previous one are three:

1. **The inclusion of rotation:** the code uses the methodology developed by Kippenhahn et al. (1970) and Meynet and Maeder (1997). The basic quantity describing the effect of rotation in the stellar structure is the angular rotation rate, ω, defined as:
$$\omega = \Omega/\Omega_{\rm crit} \ , \ \Omega_{\rm crit} = (2/3)^{3/2}\sqrt{8GM/(R_{\rm pol})^3} \tag{4.1}$$
where Ω is the angular velocity at the stellar surface and $\Omega_{\rm crit}$ is the critical angular

velocity (or breakup velocity) that is, the angular velocity at which the centrifugal force is equal to the effective gravity at the equator. G is the gravitational constant, M is the mass enclosed by $R_{\rm pol}$ that is the polar radius. Nguyen et al. (2022) considered a wide range of initial rotation rates, from non-rotating models ($\omega_{\rm i} = 0.00$) to models initially very near the critical breakup rotational velocity ($\omega_{\rm i} = 0.99$). Also worth mentioning is that in this version, rotation is enabled a few models before the Zero Age Main Sequence (ZAMS) phase. At this stage, the code computes the angular velocity Ω that corresponds to the initial rotation rate $\omega_{\rm i}$ and assigns it to each shell of the star, forcing a solid body rotation. From the ZAMS on, the solid body rotation constraint is relaxed, and the stellar rotation evolves accordingly with the conservation and the transport of angular momentum.

2. **The inclusion of mass loss during the evolution of all stars:** previously, mass loss was only considered during the stage of isochrone calculations, as it had little effect on the RGB evolution of low-mass stars, only becoming important near the tip of the red-giant branch (TRGB). Therefore, mass loss only caused a decrease in mass between the RGB and the 'zero-age horizontal branch' (ZAHB) stage, which was easily accounted for when preparing isochrones. However, with the inclusion of rotation, mass loss cannot be decoupled from evolution and must be included in all evolutionary phases because rotation can enhance mass loss and affect the star's evolutionary path. This can become drastic when the star is close to the critical breakup velocity.

3. **The treatment of turbulent mixing as a diffusive process:** while in the latter version the gas was chemically homogenised within convective regions, in the present version a diffusive approach is adopted, solving a unique equation for chemical variation due to nuclear reactions, turbulent motions, molecular diffusion, and rotational mixing.

PARSEC V2.0 takes into account masses ranging from $0.09\,M_{\odot}$ to $14\,M_{\odot}$ and metallicities between $Z = 0.004$ and $Z = 0.017$, for seven different initial rotation rates in the range $\omega_{\rm i} = 0.00 - 0.99$. Starting from the sets of evolutionary tracks isochrones are then constructed. The initial phase begins from the Pre-Main Sequence, and the final stage varies depending on the mass range of the model, with the beginning of the Thermally Pulsing Asymptotic Giant Branch (TP-AGB) phase for low- and intermediate-mass models or the C-exhaustion for higher masses. The computation of isochrones begins by selecting all the corresponding stellar tracks in each set based on their initial metallicity and rotation rate. It is worth to clarify that the isochrones are constructed for each initial rotation rate $\omega_{\rm i}$, and the deceleration of ω along the evolution is then taken into account in the tracks and tabulated within the isochrones. The construction of the isochrone then proceeds through the following steps. Initially, the computed stellar evolutionary tracks in each set are divided into phases that are uniformly separated by a few characteristic 'equivalent evolutionary points'. Afterwards, for a specific age, the isochrone is generated by interpolating all stellar properties between points of different initial mass but equivalent evolutionary stage. Isochrones are produced by the

TRILEGAL code (Girardi et al. (2005a)), which interpolates all the additional quantities needed to characterise rotating stars in the metallicity range between $Z = 0.004$ and 0.017 and in the age range $7.0 \leq log(\mathrm{t/yr}) \leq 10.1$. Moreover, the isochrones employed in the present work are calculated interpolating the rotation rate as well, in the range $0.0 \leq \omega_{\mathrm{i}} \leq 0.99$. This feature is an additional option with respect to what is described in Nguyen et al. (2022). These isochrones will soon be accessible through the following link: http:stev.oapd.inaf.it/cmd.

The intrinsic properties of stars, such as luminosity, mean effective temperature, and radius at the pole and equator, are provided by theoretical isochrones. To compare these isochrones with observed CMDs, they are supplemented with photometric magnitudes in several filters. For non-rotating stars, tables of bolometric corrections (BCs) are used as a function of effective temperature, surface gravity, and metallicity (see Girardi et al. (2002)). Bolometric correction tables for rotating stars have at least two more parameters than those for non-rotating stars: the initial rotation rate ω_{i} and the inclination angle, i, of the line of sight with respect to the stellar rotation axes (see 2.1.1). They are calculated as in Girardi et al. (2019) and implemented in the YBC database of BCs by Chen et al. (2019) and in the TRILEGAL code used in this work to produce the isochrones.

4.2 Generation of partial models

As previously stated, the final goal is to identify, for each cluster, the model that best reproduces the observations. The final model $\mathbf{M}$ is such that:

$$\mathbf{M} = PM_0 + \sum_i a_i \, PM_i \tag{4.2}$$

in analogy with Mazzi et al. (2021). Here PM_0 is the simulation for the background field of the LMC/SMC + MW foreground, as better explained in Section 4.3, while the PMs are the partial models computed each with a different rotation rate. The coefficients a_i will tell the relative importance of each PM_{i} corresponding to each ω_{i}, that is namely the distribution of the rotational velocity. Obtaining the PMs required the following steps.

From isochrones to synthetic populations

Before proceeding with generating the stellar population the isochrone needs to be corrected for extinction (A_λ) and distance modulus ($(m - M)_0$), since the isochrones by TRILEGAL (Girardi et al. (2005a)) are generated in absolute magnitudes M_{iso}, therefore at a distance of 10 *pc*. Hence, the corrected magnitude m_{iso} will be:

$$m_{iso} = M_{iso} + (m - M)_0 + A_\lambda \tag{4.3}$$

where $A_\lambda = A_V \cdot C_\lambda$, with A_V being the extinction in the V band and the C_λ being available in the YBC tables (Chen et al. (2019)). Recalling that isochrones are generated by interpolating all stellar properties between points of different initial mass but

equivalent evolutionary stage, it follows that each point on the isochrone corresponds to a specific value of colour, magnitude, and initial mass as well. Starting from the rotating isochrones stellar populations have to be generated manually. Each row of the isochrone file that is generated by TRILEGAL (Girardi et al. (2005a)) contains information on the integrated Initial Mass Function (int_IMF). For each row k of the file, $N = M_{\rm tot} \cdot (\text{int\_IMF}[\text{k}+1] - \text{int\_IMF}[\text{k}])$ stars are generated with a linear interpolation, choosing $M_{\rm tot} = 10^7 M_\odot$.

Binary stars

Within star clusters, binary stars, consisting of two stars orbiting around a common center of mass, play a significant role in shaping the properties and dynamics of the cluster. Since their presence can leave discernible signatures on the cluster's CMD, it is crucial that binary stars are taken into account. In particular, when binary stars are unresolved, i.e., their components cannot be distinguished individually, they appear as single points in the CMD, therefore the binary system appears as a single source whose light is combined together. If we consider the two components of a binary system and indicate with m_1, m_2, F_1, and F_2 their magnitudes and fluxes, the binary will appear as a single object with a magnitude:

$$m_{bin} = m_1 - 2.5 \log\Big(1 + \frac{F_2}{F_1}\Big) \tag{4.4}$$

For a binary system consisting of two main sequence (MS) stars (referred to as an MS-MS binary), the fluxes observed are directly related to the masses of the individual stars, denoted as M_1 and M_2. The luminosity of the binary is influenced by the mass ratio $q = M_2/M_1$, where it is assumed here that M_2 is smaller than M_1 (i.e., $q < 1$). In the case of equal-mass binaries, the system forms a sequence that runs nearly parallel to the MS and is approximately 0.75 mag brighter. However, when the masses of the binary components are unequal, the binary system will appear redder and brighter compared to the primary star. These systems occupy a specific region in the CMD located on the red side of the main sequence ridge line (MSRL) but below the line formed by equal-mass binaries. This is illustrated in Figure 4.1 by Milone et al. (2012), representing model MS-MS binary sequences with different mass ratios for the Globular Cluster NGC 2298, where they used their empirical MSRL and the mass-luminosity relations of Dotter et al. (2007) to generate sequences of MS-MS binary systems with different mass ratios.

When dealing with binary systems in star clusters there are two main fundamental parameters: the fraction of binaries $f_{\rm bin}$, representing the number of binary systems with respect to the total number of stars in the cluster, and the mass ratio q defined above. In this case the idea was to chose a flat distribution of the mass ratio truncated at $q_{min} = 0.7$, given that usually binary systems are clearly visible in the CMD when $q > 0.7$. To generate binary stars, a series of six steps were necessary, which are outlined as follows.

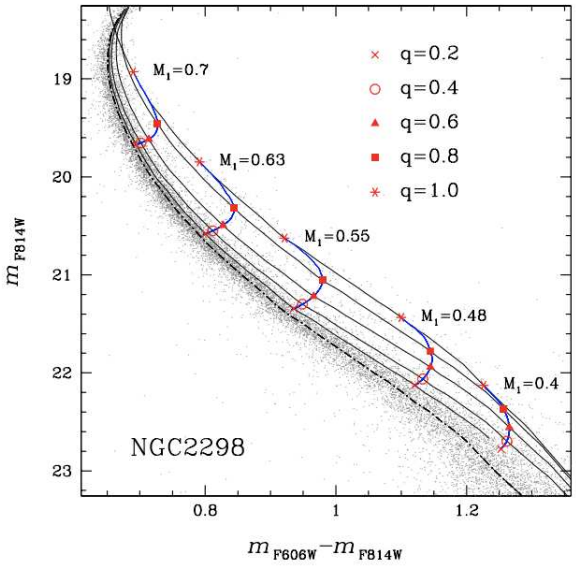

Figure 4.1: Model MS-MS binary sequences with different mass ratios for NGC 2298. The dashed-dotted line is the MSRL while, continuous black lines indicate the sequences of constant q and blue lines mark sequences of constant M_1. By Milone et al. (2012)

1. The mass of single stars generated in the previous step is obtained through linear interpolation. Indeed, as already said, each point on the isochrone corresponds to a specific value initial mass listed in the column Mini of the isochrones.
2. A random number between 0 and 1 is associated to each single star. If the random number corresponding to the specific single star is smaller than $f_{\rm bin}$ its binary companion can be generated and the procedure continues.
3. The mass ratio is defined with a flat distribution by generating another random number n between 0 and 1:

$$q = q_{min} + n \cdot (1 - q_{min}) \tag{4.5}$$

4. Once the mass of the primary star M_1, and the mass ratio q are known it is easy to retrieve the mass of the secondary star: $M_2 = q \cdot M_1$
5. The magnitude of the secondary stars m_2 is retrieved through linear interpolation.
6. Finally, the magnitude of the binary system is obtained from equation 4.4, where $F_1 = 10^{-0.4m_1}$ and $F_2 = 10^{-0.4m_2}$.

As it is illustrated in Section 4.4, the fraction of binaries $f_{\rm bin}$ is one of the parameters that are fitted with *sfhfinder*; for this reason it is required that the Hess diagrams are built separately for single and binary populations, for the same age-initial rotation rate bins, and for the same total initial mass of stars.

Distribution of inclinations

As said in Section 2.2, if stars in a cluster do not have a preferred angle of inclination, but a distribution of various inclinations, high rotating stars could be the responsible of the eMSTO phenomenon observed in CMDs. For this reason it is crucial to take into account the distribution of inclination angles to ensure the accuracy of this work. The isochrones contain the magnitudes for different values of the inclination angle. In particular, nineteen inclination angle bins are used, from 0° up to 90° with constant steps of 5°. Here the choice is to consider an unnniform distribution of inclination angles when producing the PMs. In order to pursue this a stellar population is generated, with the method explained in the subsections right above, for each value of the inclination angle, hence doing it for nineteen times considering each time the magnitude columns of the corresponding inclination. Afterwards, the Hess diagram produced for each value of the inclination angle is weighted by a probability of the type of $P \sim sin(i)$.

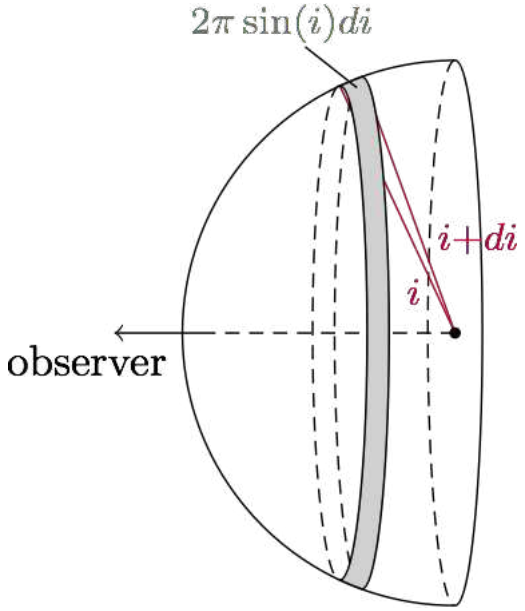

Figure 4.2: Schematic representation for the solid angle subtended by the inclination range i to $i + di$. By Burleson (2018).

This choice can be understood by looking at Figure 4.2. According to the figure, the solid angle subtended by the inclination range i to $i + di$ is $d\Omega = sin(i)didd\phi$, that is $d\Omega = 2\pi sin(i)di$. It is clear then that having a maximum probability when $i = 90°$ while minimum probability at $i = 0°$ translates into $P \sim sin(i)$, meaning that it is more likely to observe systems with high inclination angles than those pointed toward us. This means that, in order to have an isotropic distribution of inclinations, each Hess diagram corresponding to the inclination i was multiplied by the weight being:

$$weight[i] = \frac{sin(i)}{\sum_i weight[i]} \tag{4.6}$$

Finally, the resulting weighted nineteen Hess diagrams are added together. This procedure is performed for both the Hess diagrams of single stars and the Hess diagram of binary stars.

Spreading with ASTs

An observed CMD is always affected by photometric errors, blending and incompleteness, therefore it never resembles a pure isochrone. It follows that it is necessary to simulate the effects of photometric errors on our models. In order to characterize the errors in the photometry, articiaial star tests (ASTs) are performed, where artificial stars are generated across the entire CMD, covering the required sky area. The AST process gives in output a table containing the errors on the recovered magnitude (σ_m) and colour (σ_c) of each artificial star as well as a flag determining whether it is considered as recovered or lost. This information is necessary to determine how a partial model has to be spread in order to reproduce errors and incompleteness present in the data. Two main steps are needed.

The first step consists of computing the completeness map. In principle, the completeness of each cell (i,j) of the Hess diagram, can be computed from the number of artificial stars recovered in the cell divided by the number of artificial stars that were generated in it. However, the number of artificial stars in the cell might be small and lead to a bias in the result. Therefore, a slightly modified procedure is used: instead of considering just the artificial stars in the cell at position (i,j), stars in multiple cells are used, namely all those in cells with indices (k,l) such that:

$$\begin{cases} j - N_{\text{submag}} < l < j + N_{\text{submag}} \\ i - N_{\text{subcol}} < k < i + N_{\text{subcol}} \end{cases} \tag{4.7}$$

where N_{submag} and N_{subcol} are integer numbers that can be set depending on how many artificial stars have been generated. Assuming that N_{sim} artificial stars have been generated in this group of cells, but N_{obs} have been recovered, the completeness at the coordinate (i,j) of the Hess diagram is computed as

$$C_{i,j} = N_{\text{obs}}/N_{\text{sim}} \tag{4.8}$$

The second step builds, for each cell (i,j), a Hess error map. We consider the N_{obs} artificial stars introduced above, each one characterized by errors σ_c and σ_m, and treat them as if they were generated in the cell (i,j). A new coordinate can be assigned to each one to produce a new Hess diagram $E^*_{i,j}$:

$$\begin{cases} p = i + int(\sigma_c/\Delta c) \\ q = j + int(\sigma_m/\Delta m) \end{cases} \tag{4.9}$$

where Δc and Δm are the resolutions of the Hess diagram in color and magnitude, respectively. Dividing $E^*_{i,j}$ by $N_{\rm obs}$ and multiplying it by the completeness $C_{i,j}$ we determine the error map $E_{i,j}$.

$$E_{i,j} = \frac{E^*_{i,j}}{N_{\rm obs}} \cdot C_{i,j} \tag{4.10}$$

Finally, to spread a partial model PM, each one of its cells is multiplied by the corresponding error map, that is

$$\mathrm{PM}_{spr} = \sum_{i=0}^{N_{\rm c}} \sum_{j=0}^{N_{\rm m}} \mathrm{PM}(i,j) * E_{i,j} \tag{4.11}$$

where N_c and N_m are the number of cells of the Hess diagram along the color and mangitude axes, respectively. In a sense, the partial model gets convoluted with an error matrix. Figure 4.3 shows the Hess diagrams for a single model, before and after applying the results of ASTs.

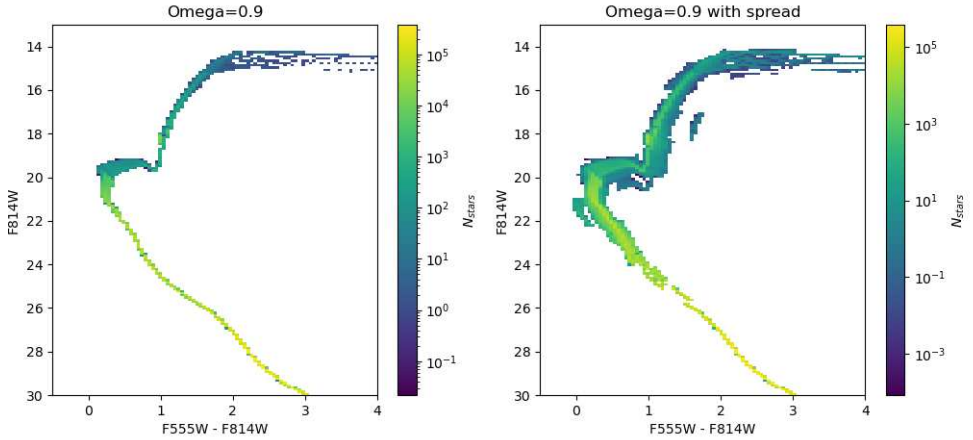

Figure 4.3: Hess diagrams for a single stellar population, before (left) and after (right) applying the results of ASTs. The model has an age $log(\mathrm{t/yr}) = 9.075$, metallicity $Z = 0.003$, $\omega_{\rm i} = 0.9$, V-band extinction $A_{\rm v} = 0.15$ mag and true distance modulus $(m - M)_0 = 18.85$ mag.

4.3 The field contribution

As stated in Equation 4.2, the final model **M** is given by the linear combination of the partial models PMs summed with PM_0. The PM_0 represents the simulation for the background field of the LMC/SMC and the MW foreground. The latter is computed with the calibrated TRILEGAL model (Girardi et al. (2005b); Girardi (2016)), while Figure 4.4 illustrates a Right Ascension (RA) - Declination (DEC) map showing the regions of the LMC (left) and SMC (right) where the Star Formation History (SFH)

is available (see Mazzi et al. (2021)) and field star simulations, performed as well with TRILEGAL, can be conducted. Specifically, this involves the simulation of ~ 0.1 square degree area surrounding the target cluster.

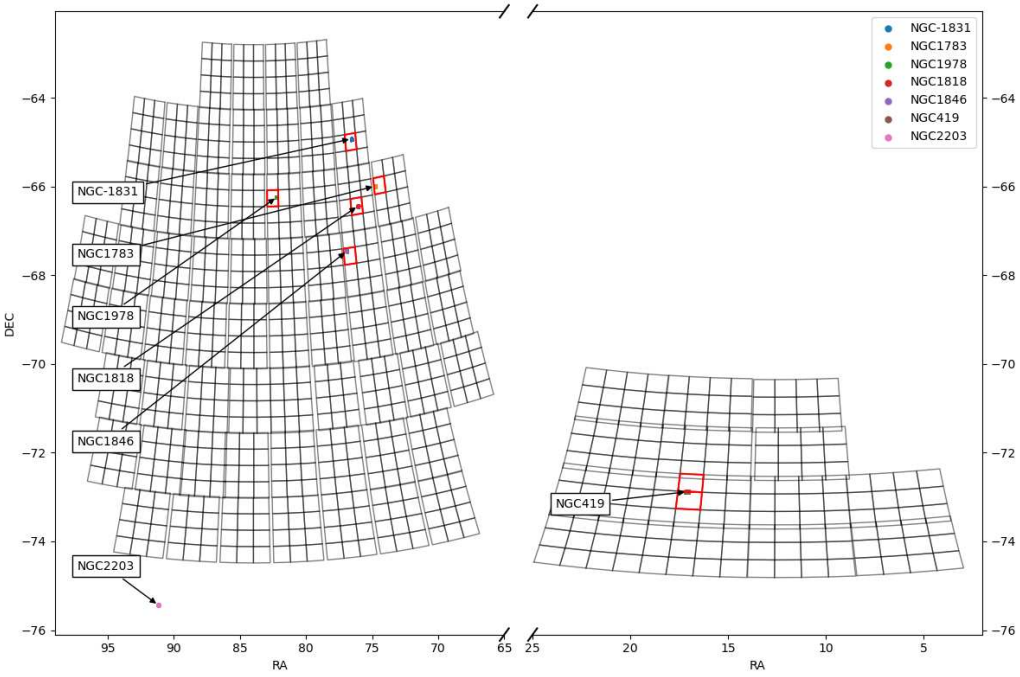

Figure 4.4: RA-DEC map with the regions of the LMC (left) and the SMC (right) for which we have the SFH. The red squares represent the simulated subregions around each cluster.

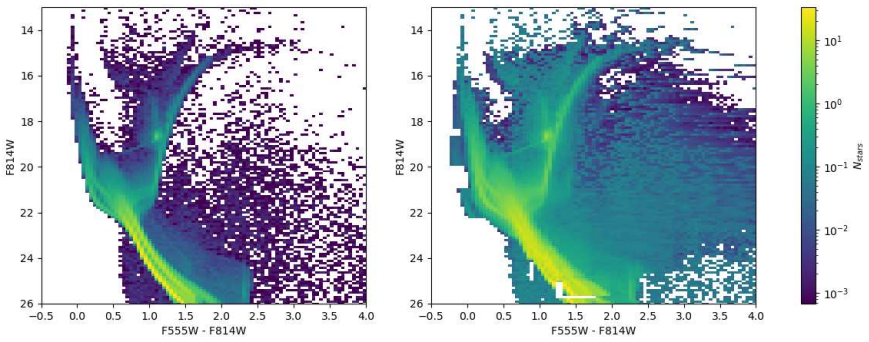

Figure 4.5: Left-hand panel: Hess diagram of the PM_0 for NGC 419 star cluster in the SMC. Right-hand panel: same as in the left hand panel after applying the spreading with ASTs.

The simulations encompass the complete extent of the regions observed by the VISTA Magellanic Clouds (VMC) Survey, that is a large-scale observational survey conducted

using the VISTA telescope (Visible and Infrared Survey Telescope for Astronomy). The photometric catalogues are split into 12 subregions per tile and the subregions are numbered from G1 to G12. The following convention is adopted: subregions are referred to as Tt_Gg, where t is an abbreviated number of the LMC/SMC tile from VMC, and g is the subregion number from 1 to 12.

Figure 4.6, taken from Mazzi et al. (2021), shows the map of the VMC tiles and subregions for the LMC, while Table 4.1 contains the name and the area of the subregion for each cluster considered in this work.

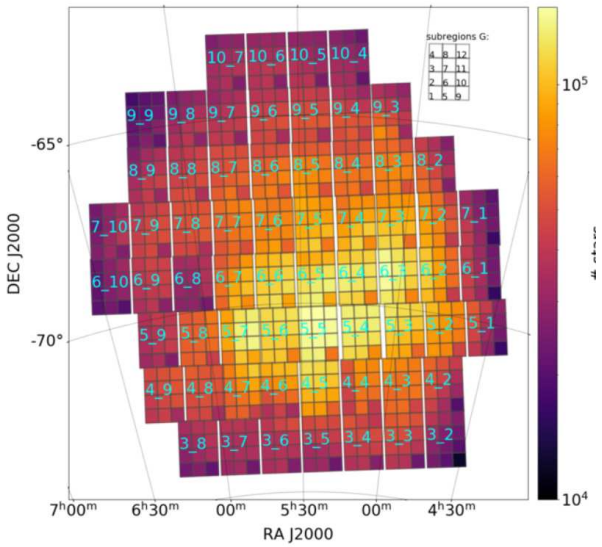

Figure 4.6: Map of the VMC tiles and subregions for the LMC. Tiles are labelled in cyan, and the inset at the top-right illustrates the numbering of the subregions from G1 to G12, which applies to all tiles. The colour scale indicates the total number of stars detected in both J and K_s filters of the VISTA Infra Red CAMera (VIRCAM) for each subregion. From Mazzi et al. (2021)

Table 4.1: Name and the area of the subregion for each cluster considered in this work. Column 1: Cluster name; Column 2: Subregion name; Column 3: Subregion area (deg^2)

Cluster name	**Subregion name**	**Subregion area**
NGC 419	T44G10 - T44G6	0.143
NGC 2203	T37G1	0.125
NGC 1831	T93G6	0.125
NGC 1866	T94G9	0.125

For the particular case of NGC 2203, that is out of the SFH maps, the closest VMC field was used. To incorporate these simulations into the fitting process, it is necessary to multiply both the SMC/LMC field and the MW foreground by a scaling factor determined by the ratio between the area of the cluster that is effectively observed by HST

and the subregion area. The rescaled simulations are then added together and converted into an Hess diagram with photometric errors simulated as described in Section 4.2.

An example of the final result is in Figure 4.5, where the Hess diagram of the PM_0 for NGC 419 star cluster in the SMC is illustrated in the left-hand panel, while in the right-hand panel the same PM_0 after applying the spreading with ASTs is shown.

4.4 Model construction with sfhfinder

The preceding sections outline the steps required to generate the essential components for constructing the final model **M**, whose Hess diagram best reproduces the Hess diagram of the observations. This is done with the *sfhfinder* code, that is conceived to derive spatially-resolved SFH, and is now applied to retrieve the distribution of stellar rotational velocities of the target clusters. In this work 4 fitting parameters were considered:

- a_i: the coefficients telling the relative importance of each partial model PM_i corresponding to a given initial rotation rate ω_i.
- f_{bin}: the binary fraction representing the number of binary systems with respect to the total number of stars.
- ΔCol: the shift in colour.
- ΔMag: the shift in magnitude.

In order to find the best-fitting parameters for a given dataset the code combines the power of optimization with Gradient Descent with Momentum and the exploration capabilities of Monte Carlo Markov Chain (MCMC). As first step the code performs iterations of the optimization process using Gradient Descent with Momentum with the aid of minimizing the $-\ln \mathrm{PLR}$ (see equation 4.17). At each iteration, the code calculates the gradients of the loss function with respect to the parameters, incorporating the momentum term to update the parameter values. This process continues until the maximum number of steps, that is initially set, is reached. However there is no warranty that the solution found is not trapped into a local minimum, hence, to find more likely solutions and estimate the errors, the code proceeds with the second step incorporating 2 MCMCs, each with an initial warmup phase allowing the method to acquaint itself with the parameter space.

4.5 Statistical comparison of the model CMD with data

In model selection, scientists commonly utilize the χ^2 statistic as a statistical indicator. The χ^2 reflects the disparity between the data and the model, taking into account the predicted 1σ error. However minimizing the χ^2 is actually a maximum-likelihood calculation for the case of data with Gaussian errors and known uncertainties at each point. Indeed, if P_i is the probability that the observation n is drawn from model m, m_i

is the model value of bin i, n_i is the observed value of bin i and σ_i is the uncertainty of bin i:

$$P_i = \sqrt{\frac{1}{2\pi\sigma_i^2}} e^{-0.5(n_i - m_i)^2/\sigma_i^2} \tag{4.12}$$

the "Gaussian Likelihood Ratio" is then defined as the ratio between the probability that observed data n_i was drawn from a model equal to m_i and the probability that it was drawn from a model equal to n_i:

$$\mathrm{GLR}_i = \sqrt{\frac{\sigma_{ni}^2}{\sigma_{mi}^2}} e^{-0.5(n_i - m_i)^2/\sigma_{mi}^2} \tag{4.13}$$

where σ_{mi} is the expected uncertainty for model m_i and σ_{ni} is the uncertainty for model n_i. Multiplying the individual Gaussian likelihood ratios and taking the logarithm the result is:

$$-2 \ln \mathrm{GLR} = \chi^2 + \sum_i ln \frac{\sigma_{mi}^2}{\sigma_{ni}^2} \tag{4.14}$$

It follows that if the observational errors follow a Gaussian distribution and the σ_i remain constant, minimizing the χ^2 is equivalent to maximizing the likelihood. However in CMD analysis, neither of these assumptions holds true. Our data is indeed characterized by a Poisson distribution, and $\sigma_{ni}^2 = n_i$ while $\sigma_{mi}^2 = m_i$, therefore using the χ^2 to minimize Poisson-distributed data poses a risk because the obtained "solution" may not be the correct one. For this reason, rather than employing a χ^2 fit, which makes certain implicit assumptions about the data, it is recommended to use a maximum likelihood parameter derived from the Poisson probability distribution:

$$P_i = \frac{m_i^{n_i}}{e^{m_i} n_i!} \tag{4.15}$$

The "Poisson likelihood ratio" is analogous to the Gaussian likelihood ratio in equation 4.13. Cancelling the $n_i!$ terms in numerator and denominator, we get the ratio of the probability of drawing n_i points from model m_i to that of drawing n_i points from model n_i:

$$\mathrm{PLR}_i = \frac{m_i^{n_i} e^{n_i}}{n_i^{n_i} e^{m_i}} \tag{4.16}$$

and the Poisson equivalent of χ^2 is:

$$-\ln \mathrm{PLR} = \sum_i m_i - n_i + n_i \, ln \frac{n_i}{m_i} \tag{4.17}$$

As stated by Dolphin (2002), considering the availability of a Poisson-based statistic that can be minimized using the same approach as χ^2, there is no valid justification for using χ^2 to fit a CMD, as it will invariably yield an incorrect solution when minimized. Therefore, minimizing equation 4.17 represents a genuine maximum likelihood computation, and employing this parameter in this study will lead to an accurate determination of the best-fit value.

Chapter 5

Results

The results obtained for each cluster considered in this work are presented in the following sections. As already described in previous chapters the final model that best-fits the observed CMD is a linear combination of the PMs, telling us the relative importance of each population corresponding to each rotational velocity. This procedure is performed for different age and metallicity bins, chosen accordingly to which cluster is being analyzed. In all cases, for each couple of age and metallicity a total amount of 11 Partial Models were produced, corresponding to 11 values of the initial rotation rate $\omega_{\rm i} = 0.0, 0.1, 0.2, 0.3, 0.4, 0.5, 0.6, 0.7, 0.8, 0.9, 0.99$.

5.1 NGC 419

As already pointed out in Section 3.1, Goudfrooij et al. (2014) found values for the age and metallicity of NGC 419 to be $t = 1.45 \pm 0.05$ Gyr and $[Fe/H] = -0.7 \pm 0.1$, respectively. Let's recall the definition of $[Fe/H]$:

$$[Fe/H] = \log\Big(\frac{Z}{X}\Big)_* - \log\Big(\frac{Z}{X}\Big)_\odot \tag{5.1}$$

where $\frac{Z}{X}$ is the metal to hydrogen mass ratio. If we approximate X to be constant, given that the variations in the helium and heavy element abundances are typically negligible with respect to the hydrogen abundance, the above equation can then be simplified into:

$$[Fe/H] = \log\Big(\frac{Z_*}{Z_\odot}\Big) \tag{5.2}$$

Given the literature value of $[Fe/H]$ for NGC 419, and adopting the solar metallicity as derived by Caffau et al. (2011) ($Z_\odot = 0.01524$), after a simple calculation we retrieve that $Z \sim 0.003$. Moreover, taking the logarithm of the cluster's age derived by Goudfrooij et al. (2014) we get $\log(\mathrm{t/yr}) \simeq 9.16$. Therefore, it was decided to produce Partial Models for 2 values of the metallicity, $Z = 0.003$ and $Z = 0.004$, and for 8 values of the age, from

$\log(\mathrm{t/yr}) = 9.000$ to $\log(\mathrm{t/yr}) = 9.175$ with constant steps of $\Delta \log(\mathrm{t/yr}) = 0.025$. The result is a total amount of 16 best-fitting models M given by equation 4.2. Moreover, in order to infer the effect of including the PM_0 model for the MCs field and MW foreground, the 16 best-fitting models were computed both with and without the PM_0, for a total of 32 best-fit models.

As anticipated in Section 4.5, given the poissonian nature of the distribution of our data, the most suitable approach to identify the best model among those 32 best-fitting models is to compute and minimize equation 4.17. The results are represented in Figure 5.1 for $Z = 0.003$ and in Figure 5.2 for $Z = 0.004$, with (red points) and without (blue points) the inclusion of the PM_0.

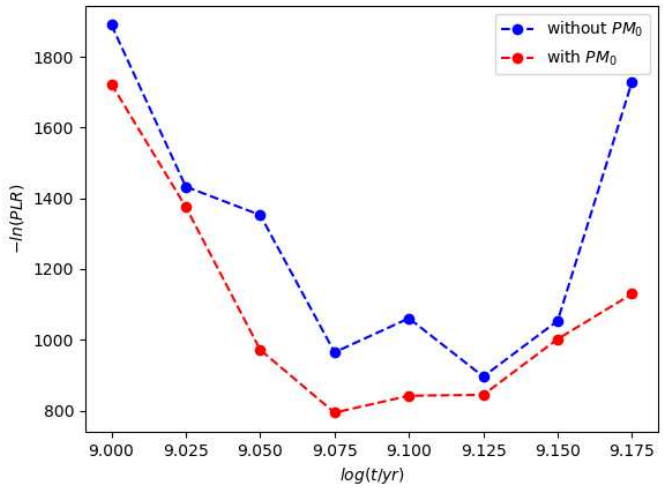

Figure 5.1: $-\ln \mathrm{PLR}$ as function of the age $\log(\mathrm{t/yr})$ for NGC 419, for a metallicity of $Z = 0.003$. Blue points represent the $-\ln \mathrm{PLR}$ of the models computed without taking into account the PM_0 for the SMC field and MW foreground. Red points correspond to the case in which the PM_0 is taken into account when computing the best-fitting models.

It is evident, for both values of the metallicity, that the models including the PM_0 are better than the ones without the PM_0, at all ages. Hence, this demonstrate the positive effect of the inclusion of a model for the field and foreground for this cluster. The results of the computation of the $-\ln \mathrm{PLR}$ are summarized in Table 5.1 and suggest that the best model is the one corresponding to a metallicity of $Z = 0.003$ and age $log(\mathrm{t/yr}) = 9.075$.

The Hess diagram of this best-fitting model is represented in Figure 5.3, together with the Hess diagram of the observation, the residuals and the normalized residuals. As we are mainly interested in providing the fit in the regions of the eMSTO and RC, a mask was applied cutting for $14 < F814W < 21.5$ and $-0.5 < F555W - F814W < 3$. Additionally, Figure 5.4 displays a zoom on the RC region . Looking at these figures it

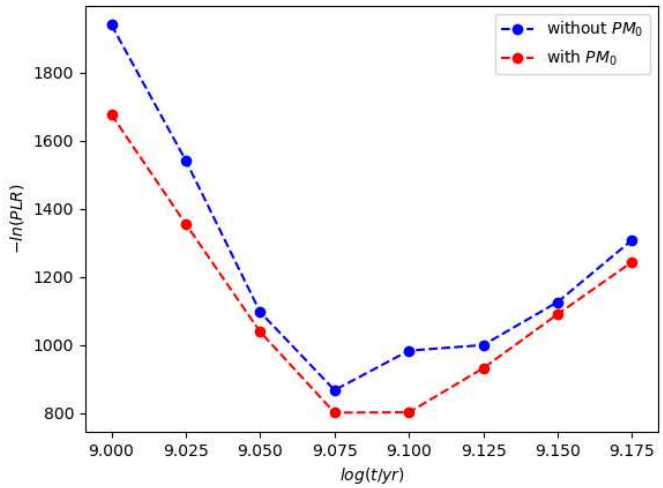

Figure 5.2: $-\ln$PLR as function of the age log(t/yr) for NGC 419, for a metallicity of $Z = 0.004$. Blue points represent the $-\ln$PLR of the models computed without taking into account the PM_0 for the SMC field and MW foreground. Red points correspond to the case in which the PM_0 is taken into account when computing the best-fitting models.

Table 5.1: Best-fit parameters obtained minimizing the quantity $-\ln$PLR for NGC 419. Column 1: Metallicity Z; Column 2: Inclusion of the PM_0; Column 3: log(Best Age/yr); Column 4: $-\ln$(PLR).

Metallicity	PM_0	Best Age	$-\ln$PLR
0.003	**yes**	**9.075**	**793.89**
0.003	no	9.075	964.50
0.004	yes	9.075	801.57
0.004	no	9.075	867.77

appears that the analysis provides a very good fit at the level of the MSTO, where the residuals are close to zero. Moreover, the model exhibits a fairly extended RC region, although some negative residuals are present and are clearly visible in the third panel. This may suggest that relying solely on stellar rotation might not be sufficient to replicate the full extension of the RC in NGC 419.

As previously pointed out in Section 4.4, *sfhfinder* code is used to provide the best-fit values of 4 parameters. In Table 5.2 are reported the best-fit values of the binary fraction f_{bin}, the shift in colour $\Delta(F555W - F814W)$, and the shift in magnitude $\Delta F814W$ as provided by *sfhfinder* for the $Z = 0.003$ and log(t/yr) = 9.075 model.

The best-fit values of the a_i coefficients of equation 4.2, along with the 1σ confidence interval, are listed in Table 5.3 and are plotted in Figure 5.5, which specifically represents the distribution of stellar rotational velocities of NGC 419. It is shown that this cluster

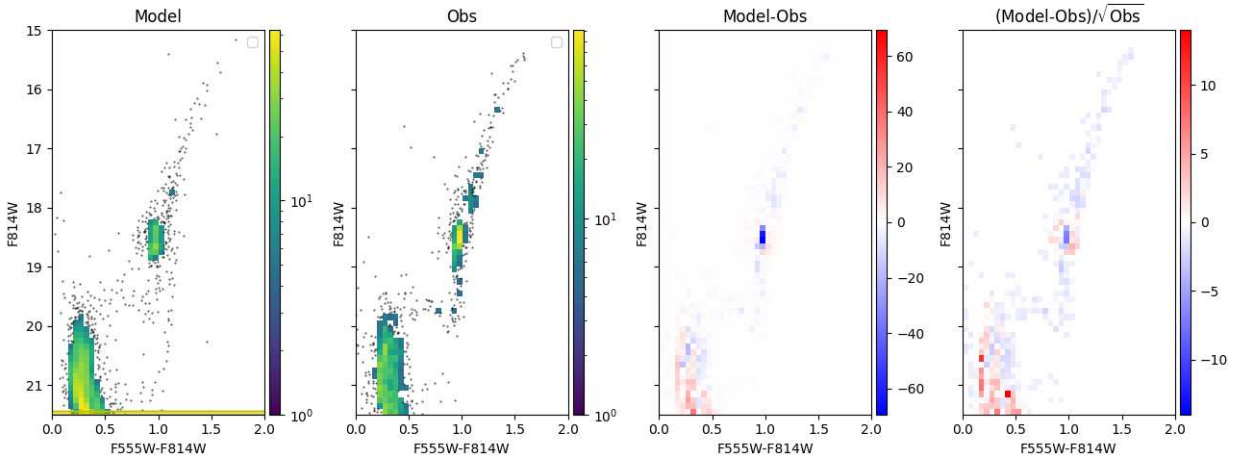

Figure 5.3: Left-hand panel: Hess diagram of the best-fitting model corresponding to a metallicity of $Z = 0.003$ and age $\log(\mathrm{t/yr}) = 9.075$. Second panel: Hess diagram of the observation of NGC 419 obtained with the ACS of the HST. Third panel: residuals. Right-hand panel: normalized residuals.

Table 5.2: Best-fit values of the binary fraction f_{bin}, the shift in colour $\Delta(F555W - F814W)$, and the shift in magnitude $\Delta F814W$ for NGC 419.

f_{bin}	0.200 ± 0.012
$\Delta(F555W - F814W)$	0.012 ± 0.001 mag
$\Delta F814W$	0.245 ± 0.005 mag

harbors stars with $\omega_{\mathrm{i}} > 0.9$, with a tiny fraction of stars with $\omega_{\mathrm{i}} = 0.8$ and a negligible amount of stars with $\omega_{\mathrm{i}} < 0.8$. The comprehensive analysis performed on NGC 419 ultimately suggests that the morphology observed in its CMD, with its distinct features, can be thoroughly accounted for by the presence and influence of extreme rotators among its stellar population.

5.2 NGC 2203

The analysis for NGC 2203 proceeded in a very similar way. This cluster is slightly older with respect to NGC 419 and it is located in a different environment, namely the LMC, with different metallicity. According to Goudfrooij et al. (2014), the age and metallicity of this cluster are, respectively, $t = 1.55 \pm 0.05$ Gyr and $[Fe/H] = -0.3 \pm 0.1$. For this reason the analysis was conducted for 2 sets of metallicity, $Z = 0.007$ and $Z = 0.008$, and 8 values of the age from $\log(\mathrm{t/yr}) = 9.100$ to $\log(\mathrm{t/yr}) = 9.275$ with constant steps of $\Delta \log(\mathrm{t/yr}) = 0.025$, hence resulting in 16 best-fitting models. Also in this case each best-fitting model was computed for the 2 cases, with and without the PM_0. The results are represented in Figure 5.6 for $Z = 0.007$ and in Figure 5.7 for $Z = 0.008$, with (red points) and without (blue points) the inclusion of the PM_0.

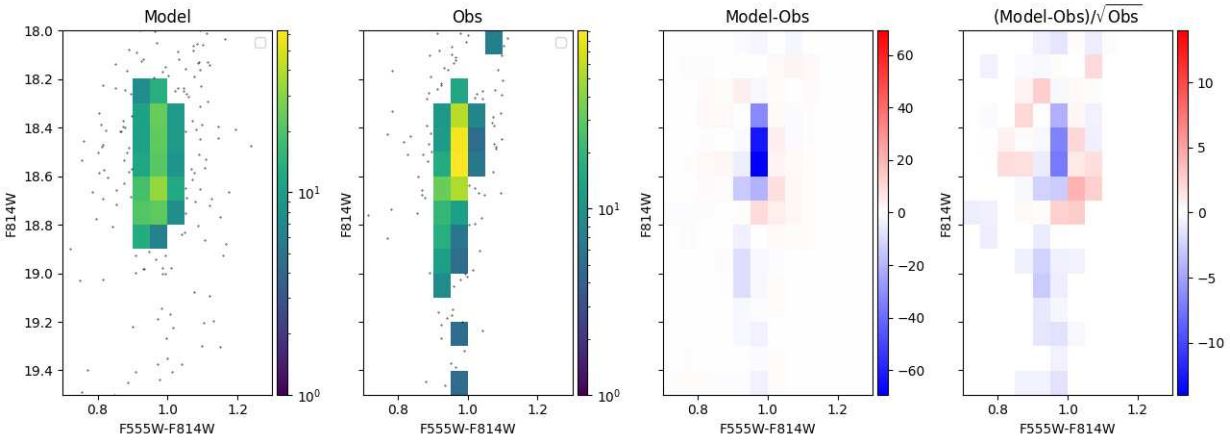

Figure 5.4: Same as Figure 5.3 but with a zoom on the RC region.

Table 5.3: Best-fit values of a_i coefficients for NGC 419.

Coefficient	Corresponding ω_i	Best-fit value	1σ confidence interval
a_1	0.0	$2.14 \cdot 10^{-5}$	$1.91 \cdot 10^{-5}$
a_2	0.1	$1.96 \cdot 10^{-5}$	$1.84 \cdot 10^{-5}$
a_3	0.2	$1.82 \cdot 10^{-5}$	$1.73 \cdot 10^{-5}$
a_4	0.3	$1.76 \cdot 10^{-5}$	$1.62 \cdot 10^{-5}$
a_5	0.4	$1.42 \cdot 10^{-5}$	$1.49 \cdot 10^{-5}$
a_6	0.5	$1.30 \cdot 10^{-5}$	$1.30 \cdot 10^{-5}$
a_7	0.6	$1.44 \cdot 10^{-5}$	$1.38 \cdot 10^{-5}$
a_8	0.7	$1.96 \cdot 10^{-5}$	$1.92 \cdot 10^{-5}$
a_9	0.8	$7.89 \cdot 10^{-5}$	$7.38 \cdot 10^{-5}$
a_{10}	0.9	0.0023	$1.42 \cdot 10^{-4}$
a_{11}	0.99	0.0022	$1.18 \cdot 10^{-4}$

In this case, for both values of the metallicity, the impact of including the PM_0 is not as clear as in the previous example of NGC 419. In both cases the difference between the red and blue points at the best age ($log(t/yr) = 9.175$) is quite small. This is explained by the fact that this cluster is a distant outlier of the LMC, hence the field contamination is almost negligible. Numerical results are listed in Table 5.4, suggesting the best-fitting model to be the one with $Z = 0.008$ and $log(t/yr) = 9.175$.

For the same reasons explained above, a mask was applied cutting for $14 < F814W < 21.5$ and $-0.5 < F475W - F814W < 3$. Figure 5.3 displays zoomed-in Hess diagrams of the best-fitting model with $Z = 0.008$ and $log(t/yr) = 9.175$, of the observation, of the residuals and normalized residuals. Additionally, Figure 5.9 shows zoomed-in Hess diagrams. The comparison between the final model and the observation suggest that the fit is overall very good, which is also confirmed by the relatively low residuals.

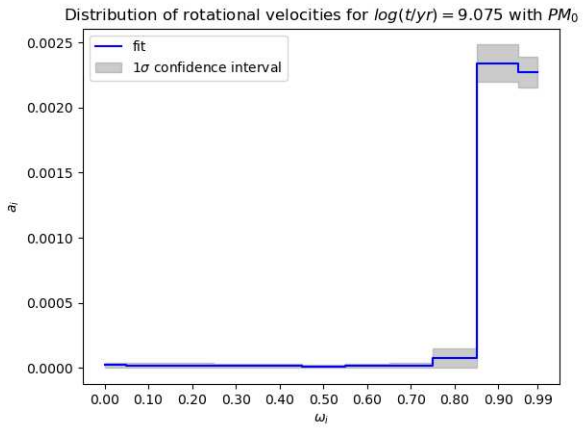

Figure 5.5: Plot of the best-fit values of the a_i coefficients for NGC 419 as function of the initial rotation rate $\omega_{\rm i}$. Grey boxes represent the 1σ confidence interval.

Table 5.4: Best-fit parameters obtained minimizing the quantity $-\ln$PLR for NGC 2203. Column 1: Metallicity Z; Column 2: Inclusion of the PM_0; Column 3: log(Best Age/yr); Column 4: $-\ln$(PLR).

Metallicity	PM_0	Best Age	$-\ln$PLR
0.007	yes	9.175	539.87
0.007	no	9.175	555.49
0.008	**yes**	**9.175**	**376.25**
0.008	no	9.175	406.52

The MSTO is well reproduced while, in analogy with the previous cluster, there is a negative residual at the level of the RC, even though NGC 2203 is not characterized by a prominent double RC as in the case of NGC 419. In Table 5.5 are reported the best-fit values of the binary fraction f_{bin}, the shift in colour $\Delta(F475W-F814W)$, and the shift in magnitude $\Delta F814W$ as provided by *sfhfinder* for the $Z=0.008$ and $\log(\mathrm{t/yr})=9.175$ model.

Table 5.5: Best-fit values of the binary fraction f_{bin}, the shift in colour $\Delta(F475W-F814W)$, and the shift in magnitude $\Delta F814W$ for NGC 2203.

f_{bin}	0.105 ± 0.011
$\Delta(F475W-F814W)$	-0.088 ± 0.002 mag
$\Delta F814W$	0.167 ± 0.005 mag

The best-fit values of the a_i coefficients of equation 4.2 and the relative 1σ confidence interval, are listed in Table 5.6 and are plotted in Figure 5.10, which depicts the distribution of stellar rotational velocities of NGC 2203. Contrary to NGC 419, this cluster doesn't include stars that are extremely close to the breakup velocity, on the other side

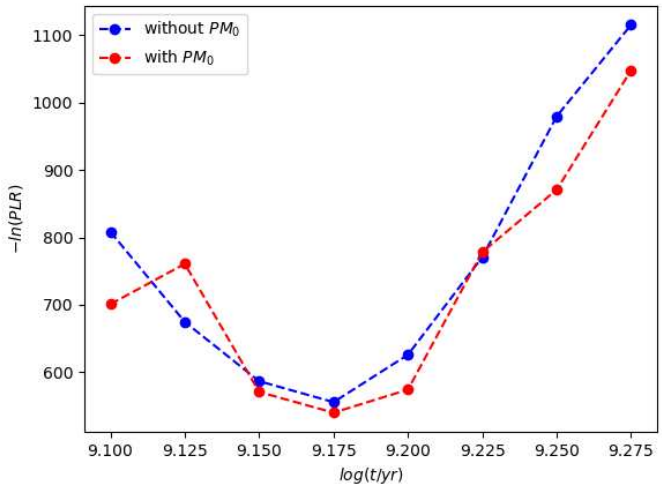

Figure 5.6: $-\ln$PLR as function of the age log(t/yr) for NGC 2203, for a metallicity of $Z = 0.007$. Blue points represent the $-\ln$PLR of the models computed without taking into account the PM_0 for the LMC field and MW foreground. Red points correspond to the case in which the PM_0 is taken into account when computing the best-fitting models.

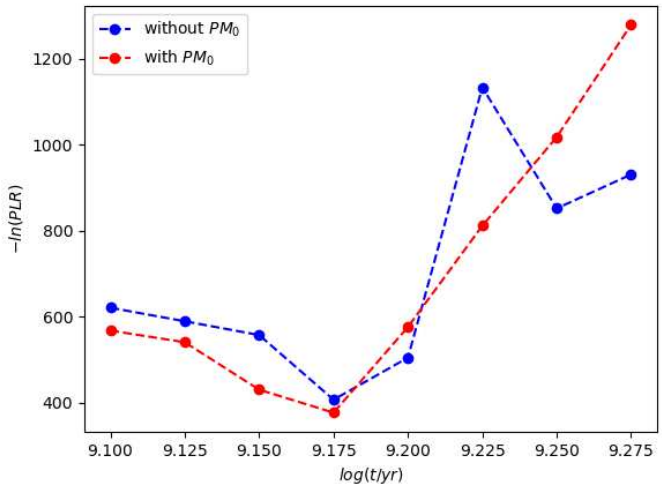

Figure 5.7: $-\ln$PLR as function of the age log(t/yr) for NGC 2203, for a metallicity of $Z = 0.008$. Blue points represent the $-\ln$PLR of the models computed without taking into account the PM_0 for the LMC field and MW foreground. Red points correspond to the case in which the PM_0 is taken into account when computing the best-fitting models.

it seems to be mainly populated by stars with $0.7 < \omega_i < 0.9$, with an almost negligible fraction of stars with $\omega_i = 0.0, 0.5$ and 0.6. Therfore, the analysis for NGC 2203 seems

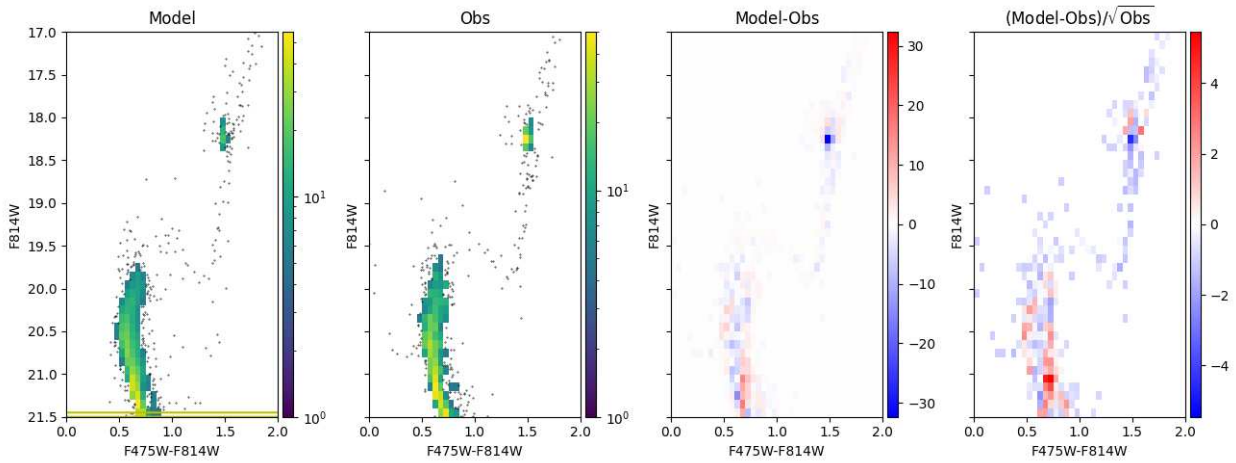

Figure 5.8: Left-hand panel: Hess diagram of the best-fitting model corresponding to a metallicity of $Z = 0.008$ and age $\log(\mathrm{t/yr}) = 9.175$. Second panel: Hess diagram of the observation of NGC 2203 obtained with the ACS of the HST. Third panel: residuals. Right-hand panel: normalized residuals.

to suggest a single population of moderate-fast rotators with $\omega_{\mathrm{i}} > 0.7$.

This cluster was also studied by Gossage et al. (2019), trying to state which scenario (pure rotation, age spread or combination of both) could reproduce the eMSTO morphology in different clusters. According to them, NGC 2203 is among the worst-fit clusters of the analysis together with NGC 1866. Moreover this was the case in which an age spread outperformed significantly the pure rotation model. As already anticipated in previous chapters, our work aims to reproduce the morphology of the CMDs of our four target clusters only assuming a pure rotation scenario. Contrary to Gossage et al. (2019), our analysis for NGC 2203 seems to give the best fit among all other clusters and the features of its CMD are well explained by the presence of moderate and fast rotators.

5.3 NGC 1831

NGC 1831 is younger ($\sim$ 800 Myr old) with respect to the first two clusters of this analysis. Goudfrooij et al. (2018) found its metallicity to be $[Fe/H] = -0.25$, corresponding to $Z \sim 0.008$. The analysis was performed for 2 sets of metallicity, $Z = 0.007$ and $Z = 0.008$, and 8 values of the age from $\log(\mathrm{t/yr}) = 8.800$ to $\log(\mathrm{t/yr}) = 8.875$ with constant steps of $\Delta \log(\mathrm{t/yr}) = 0.025$, for a total of 16 best-fitting models. As in the previous cases each best-fitting model was computed for the 2 cases, with and without the PM_0.

The first attempt to study this cluster was similar to the previous two, as it involved using a mask to isolate the region of interest. In this specific case the mask was chosen such that the fit was performed only for magnitude $23 < F814W < 16$, and colour

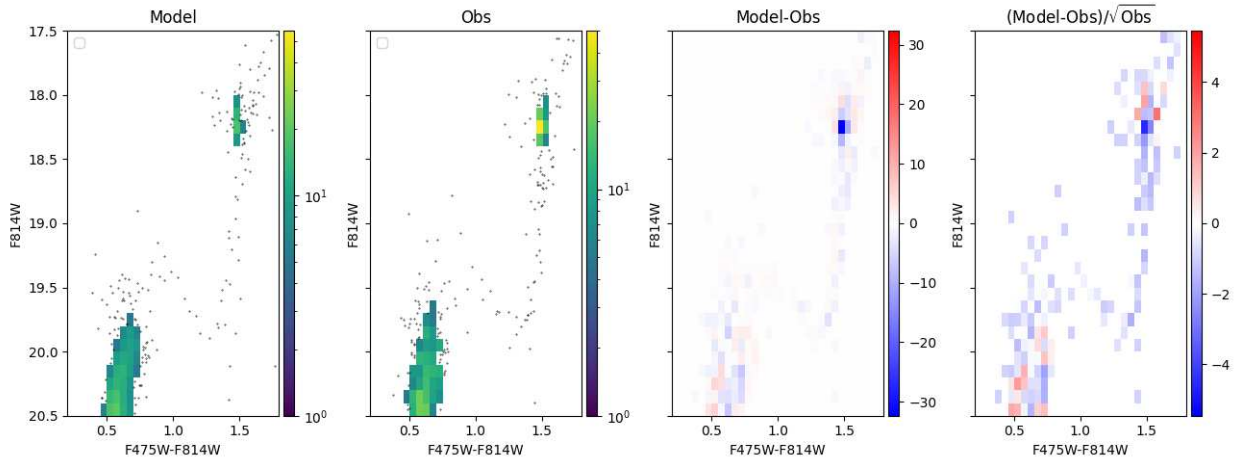

Figure 5.9: Same as Figure 5.8, but with a zoom on the TO region.

$0.0 < F336W - F814W < 3$. The best-fitting model resulting from this first analysis has a metallicity $Z = 0.007$ and age $log(\mathrm{t/yr}) = 8.850$. The top panels of Figure 5.11 show the Hess diagram of this model, together with the Hess diagram of the observation, the residuals and the normalized residual, while the bottom panels represent a zoom on the MS region. From this plot it is noticeable that, at $F814W \sim 21$, there is an excess of very bright stars in the fitted model. In order to infer which kind of stars populate this overabundant region, two PARSEC isochrones with $i = 90°$, one for $\omega_{\mathrm{i}} = 0.0$ (in pink) and the other for $\omega_{\mathrm{i}} = 0.99$ (in red), are plotted on top of the Hess diagrams. This figure shows that the stars causing an overabundance in the model are non-rotating stars, and this overabundance is precisely at the level of the MS kink. Indeed, section 3.6 provides a description of the feature known as the MS kink that characterizes the CMD of young stellar clusters, including NGC 1831. Moreover, it is also explained how this feature is artificially introduced, when computing PARSEC isochrones, with a gradual growth of rotation along an initial mass interval of $\Delta M_i = 0.3 M_{\odot}$. Hence, it may be possible that the slightly rough way in which the transition from non-rotating to rotating stars is implemented could compromise the fit in the region at the level of the MS kink. For this reason it was finally decided to apply a mask that excludes this area, cutting in magnitude for $16 < F814W < 20.5$ and $22 < F814W < 24$, and in colour for $-0.5 < F336W - F814W < 3$.

The results of the analysis performed with the new mask are presented in Figure 5.12 for $Z = 0.007$ and in Figure 5.13 for $Z = 0.008$, with (red points) and without (blue points) the inclusion of the PM_0. Consistently with the analysis of NGC 419, also in this case the effect of including the PM_0 is to improve the fit at all ages and for both values of the metallicity.

Numerical values of $-\ln \mathrm{PLR}$ corresponding to the best age, for both metallicities and both options for the PM_0, are summarized in Table 5.7. The analysis indicates that

Table 5.6: Best-fit values of a_i coefficients for NGC 2203.

Coefficient	Corresponding ω_i	Best-fit value	1σ confidence interval
a_1	0.0	$5.86 \cdot 10^{-5}$	$4.25 \cdot 10^{-5}$
a_2	0.1	$3.63 \cdot 10^{-5}$	$3.33 \cdot 10^{-5}$
a_3	0.2	$2.83 \cdot 10^{-5}$	$2.64 \cdot 10^{-5}$
a_4	0.3	$2.48 \cdot 10^{-5}$	$2.27 \cdot 10^{-5}$
a_5	0.4	$2.84 \cdot 10^{-5}$	$2.68 \cdot 10^{-5}$
a_6	0.5	$5.17 \cdot 10^{-5}$	$4.96 \cdot 10^{-5}$
a_7	0.6	$5.09 \cdot 10^{-5}$	$4.58 \cdot 10^{-5}$
a_8	0.7	$9.34 \cdot 10^{-4}$	$1.68 \cdot 10^{-4}$
a_9	0.8	$4.03 \cdot 10^{-4}$	$2.05 \cdot 10^{-4}$
a_{10}	0.9	$7.00 \cdot 10^{-4}$	$1.34 \cdot 10^{-4}$
a_{11}	0.99	$3.18 \cdot 10^{-5}$	$2.73 \cdot 10^{-5}$

the model which provides the best-fit of NGC 1831 corresponds to $Z = 0.007$ and $log(\mathrm{t/yr}) = 8.875$. It should be noticed that applying the new mask that excludes the MS kink plays a role in changing the age of the best-fitting model.

Table 5.7: Best-fit parameters obtained minimizing the quantity $-\ln \mathrm{PLR}$ for NGC 1831. Column 1: Metallicity Z; Column 2: Inclusion of the PM_0; Column 3: log(Best Age/yr) in Gyr; Column 4: $-\ln(\mathrm{PLR})$.

Metallicity	PM_0	Best Age	$-\ln \mathrm{PLR}$
0.007	**yes**	**8.875**	**1145.72**
0.007	no	8.875	1165.32
0.008	yes	8.875	1264.34
0.008	no	8.900	1297.08

The Hess diagram of the new best-fitting model, the Hess diagram of the observation, the residuals and the normalized residuals are plotted in Figure 5.14, while a zoom on the MS is presented in Figure 5.15. Comparing Figure 5.14 with Figure 5.11 it seems that the fit is improved by applying the new mask that excludes the MS kink region. Moreover, it appears that the MSTO of the model is slightly shifted towards higher luminosity and hotter temperature with respect to the MSTO of the observation, while the stars belonging to the red clump are distributed along a wider range of luminosities than expected. Given that we explored two values of metallicity and eight different ages it is unlikely that this effect is due to a wrong assumption on one of these two parameters. One possibile reason could reside in the assumption of having stars with a uniform distribution of inclinations. We know from Chapter 2 that if a rotating star is viewed pole-on it will appear brighter and hotter with respect to the same star viewed equator-on, and this is also illustrated in Figure 2.5. Therefore, the model might be overestimating stars with a pole-on configuration in comparison to the observations, and

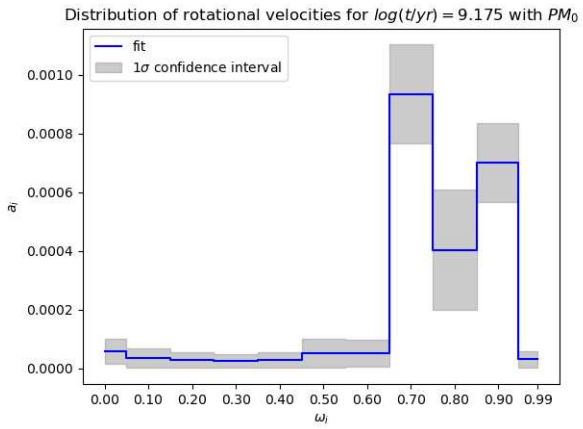

Figure 5.10: Plot of the best-fit values of the a_i coefficients for NGC 2203 as function of the initial rotation rate $\omega_{\rm i}$. Grey boxes represent the 1σ confidence interval.

the cluster's inclination distribution may not be uniform, potentially it may even be characterized by a single value of the inclination angle, due to a possible spin alignment of the stars. Hence, for future works, it could be interesting to assume a different distribution for the inclination angle.

In Table 5.8 are reported the best-fit values of the binary fraction f_{bin}, the shift in colour $\Delta(F336W - F814W)$, and the shift in magnitude $\Delta F814W$ as provided by *sfhfinder* for the $Z = 0.007$ and $\log(\mathrm{t/yr}) = 8.875$ model.

Table 5.8: Best-fit values of the binary fraction f_{bin}, the shift in colour $\Delta(F336W - F814W)$, and the shift in magnitude $\Delta F814W$ for NGC 1831.

f_{bin}	0.176 ± 0.009
$\Delta(F336W - F814W)$	-0.032 ± 0.002 mag
$\Delta F814W$	0.165 ± 0.005 mag

Table 5.9 presents the best-fit values of the a_i coefficients of Equation 4.2, together with the 1σ confidence interval, while Figure 5.16 finally illustrates the distribution of stellar rotational velocities of NGC 1831. NGC 1831 stands out as the only cluster where a discernible, although very small, group of stars exhibits $\omega_{\rm i} \lesssim 0.5$. Moreover this cluster harbor a stellar population of moderate-fast rotators with $\omega_{\rm i} > 0.7$, with the majority of its stars that are very close to the breakup velocity, similar to the case observed in NGC 419.

Correnti et al. (2021) studied this cluster comparing its CMD morphology with Monte Carlo simulations involving synthetic star clusters consisting of multiple populations with different ages or single population with a range of rotational velocities. They were able to infer that the morphology of NGC 1831 could be fully explained, within the context

of a pure rotation scenario, assuming a bimodal distribution for the rotating stars, with $\sim 40\%$ of slow rotators and the remaining $\sim 60\%$ being fast rotators. Although NGC 1831 shows a tiny fraction of stars with $\omega_{\rm i} \sim 0.4$ our analysis seems to suggest a higher fraction of fast and extreme rotators with respect to Correnti et al. (2021).

Table 5.9: Best-fit values of a_i coefficients for NGC 1831.

Coefficient	Corresponding $\omega_{\rm i}$	Best-fit value	1σ confidence interval
a_1	0.0	$6.87 \cdot 10^{-5}$	$6.12 \cdot 10^{-5}$
a_2	0.1	$6.32 \cdot 10^{-5}$	$5.77 \cdot 10^{-5}$
a_3	0.2	$8.16 \cdot 10^{-5}$	$7.13 \cdot 10^{-5}$
a_4	0.3	$6.50 \cdot 10^{-5}$	$5.78 \cdot 10^{-5}$
a_5	0.4	$1.89 \cdot 10^{-4}$	$1.15 \cdot 10^{-4}$
a_6	0.5	$6.92 \cdot 10^{-5}$	$6.00 \cdot 10^{-5}$
a_7	0.6	$4.50 \cdot 10^{-5}$	$4.14 \cdot 10^{-5}$
a_8	0.7	$2.20 \cdot 10^{-4}$	$7.97 \cdot 10^{-5}$
a_9	0.8	$1.02 \cdot 10^{-3}$	$1.02 \cdot 10^{-4}$
a_{10}	0.9	$2.58 \cdot 10^{-4}$	$1.03 \cdot 10^{-4}$
a_{11}	0.99	$1.19 \cdot 10^{-3}$	$8.82 \cdot 10^{-5}$

5.4 NGC 1866

According to Goudfrooij et al. (2018) the age of NGC 1866 is around 250 Myr, making it the youngest cluster of this study. Gossage et al. (2019), adopted a metallicity $[Fe/H] = -0.36$, based on Asplund et al. (2009) protosolar abundances, hence corresponding to $Z \sim 0.006$. The analysis encompassed two sets of metallicity, $Z = 0.006$ and $Z = 0.007$, and considered eight age values ranging from $\log(\mathrm{t/yr}) = 8.400$ to $\log(\mathrm{t/yr}) = 8.575$, with a constant step of $\Delta \log(\mathrm{t/yr}) = 0.025$. This resulted in a total of sixteen best-fitting models. Similarly to previous cases, each best-fitting model was computed twice, once including the PM_0 and once without it.

The results are represented in Figure 5.17 for $Z = 0.006$ and in Figure 5.18 for $Z = 0.007$, with (red points) and without (blue points) the inclusion of the PM_0.

In this case, the impact of including the PM_0 is positive in correspondence of the best age, for both values of the metallicity. Particularly, for $Z = 0.007$ the inclusion of the PM_0 is actually very effective. Numerical results are listed in Table 5.10, suggesting the best-fitting model to be the one with $Z = 0.007$ and $log(\mathrm{t/yr}) = 8.500$.

The Hess diagram of this best-fitting model is represented in Figure 5.19, together with the Hess diagram of the observation, the residuals and the normalized residuals. As we are mainly interested in providing the fit in the regions of the eMSTO and MS, a mask was applied cutting for $14 < F814W < 22$ and $-1.0 < F336W - F814W < 2$. Additionally, Figure 5.20 displays a zoom on the MS region. The first thing to notice is

Table 5.10: Best-fit parameters obtained minimizing the quantity $-\ln \mathrm{PLR}$ for NGC 1866. Column 1: Metallicity Z; Column 2: Inclusion of the PM_0; Column 3: log(Best Age/yr); Column 4: $-\ln(\mathrm{PLR})$.

Metallicity	PM_0	Best Age	$-\ln \mathrm{PLR}$
0.006	no	8.500	342.09
0.006	no	8.475	346.90
0.007	**yes**	**8.500**	**332.65**
0.007	no	8.500	357.47

that, unlike other clusters, there were very few data available in this case. Specifically, the circular area centered on the cluster with a radius of 35 arcsec contains a total amount of 795 stars, which is quite low and could potentially compromise the statistical analysis. Unlike the study by Gossage et al. (2019), where the fit of the eMSTO in NGC 1866 assuming a pure rotation scenario was the least accurate among the three possible scenarios, the best fitting model in this study provides a quite good reproduction of the eMSTO in NGC 1866. Moreover, the model shows less stars in the blue part of the MS, especially for $F814W \lesssim 21$, hence not fully reproducing the peculiar split MS of NGC 1866. Referring back to the explanation of the split MS in Section 1.3.2, if this distinctive feature is identified in the CMD of a stellar cluster then we expect to find a portion of slow-rotating stars that populate the blue MS and a fraction of fast and extreme rotators concentrated in the red part of the MS. However, looking at Figure 5.21, which represents the distribution of stellar rotational velocities of the best-fitting model for NGC 1866, we clearly see that the presence of stars rotating with $\omega_{\mathrm{i}} < 0.6$ is negligible, while only fast and extreme rotators seem to populate this cluster. Either the code encountered challenges in replicating the split MS, potentially due to the limited statistic, or the presence of a split MS in this cluster might not be linked to stellar rotation. However, the Bayesian analysis performed by Costa et al. (2019) on NGC 1866 clearly shows that the younger population is mainly made of slowly rotating stars and settles in the blue part of the MS, while the older one consists of fast rotators and populates the red MS. Given that slow-rotating stars of the blue MS are generally lower in number with respect to the red MS fast rotating population it is plausible that, owing to the limited statistical sample, our analysis might have exclusively captured the red MS's fast-rotators. Moreover, Costa et al. (2019) found an age separation of ~ 112 Myr between the blue MS stars and the stars belonging to the red MS, while in this work we adopt a "pure rotation scenario", assuming that all PMs have the same age. Hence, this assumption could be the reason of the discrepancy between our results and literature and NGC 1866 may indeed host multiple populations. For future works it could be interesting to perform the same analysis on other clusters that exhibit a split MS and see whether this issue arises in those cases as well.

Table 5.11 presents the best-fit values for the binary fraction f_{bin}, the colour shift $\Delta(F336W-F814W)$, and the magnitude shift $\Delta F814W$ for the $Z = 0.007$ and $\log(\mathrm{t/yr}) = 8.850$ model, while Table 5.12 contains the best-fit values of the a_i coefficients of equation

4.2 and the relative 1σ confidence interval.

Table 5.11: Best-fit values of the binary fraction f_{bin}, the shift in colour $\Delta(F336W - F814W)$, and the shift in magnitude $\Delta F814W$ for NGC 1866.

f_{bin}	0.085 ± 0.017
$\Delta(F336W - F814W)$	-0.133 ± 0.004 mag
$\Delta F814W$	0.067 ± 0.012 mag

Table 5.12: Best-fit values of a_i coefficients for NGC 1866.

Coefficient	Corresponding ω_{i}	Best-fit value	1σ confidence interval
a_1	0.0	$4.04 \cdot 10^{-6}$	$3.85 \cdot 10^{-6}$
a_2	0.1	$4.15 \cdot 10^{-6}$	$3.97 \cdot 10^{-6}$
a_3	0.2	$4.29 \cdot 10^{-6}$	$4.13 \cdot 10^{-6}$
a_4	0.3	$4.31 \cdot 10^{-6}$	$4.40 \cdot 10^{-6}$
a_5	0.4	$5.93 \cdot 10^{-6}$	$5.41 \cdot 10^{-6}$
a_6	0.5	$6.35 \cdot 10^{-6}$	$5.86 \cdot 10^{-6}$
a_7	0.6	$1.35 \cdot 10^{-5}$	$1.09 \cdot 10^{-5}$
a_8	0.7	$2.46 \cdot 10^{-5}$	$1.61 \cdot 10^{-5}$
a_9	0.8	$2.31 \cdot 10^{-5}$	$1.77 \cdot 10^{-5}$
a_{10}	0.9	$1.18 \cdot 10^{-4}$	$3.54 \cdot 10^{-5}$
a_{11}	0.99	$2.61 \cdot 10^{-4}$	$3.51 \cdot 10^{-5}$

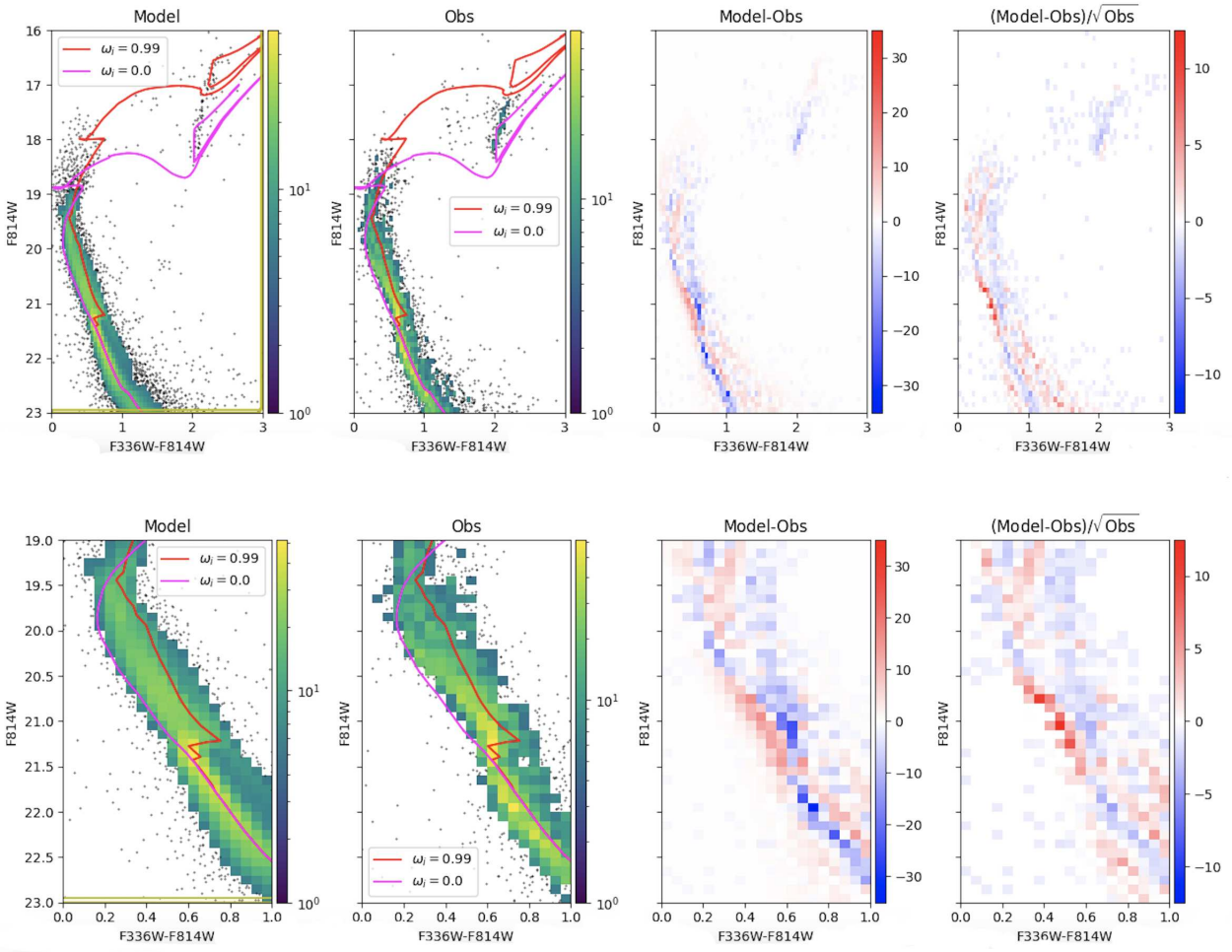

Figure 5.11: Top panels, from left to right: Hess diagram of the best-fitting model corresponding to a metallicity of $Z = 0.007$ and age $\log(t/yr) = 8.850$, Hess diagram of the observation of NGC 1831 obtained with the WFC3 of the HST, residuals and normalized residuals. Bottom panels: same as top panels but zoomed on the MS region. The overplotted PARSEC isochrones correspond to $\omega_i = 0.0$ (in pink) and $\omega_i = 0.99$ (in red), both computed with an inclination $i = 90°$.

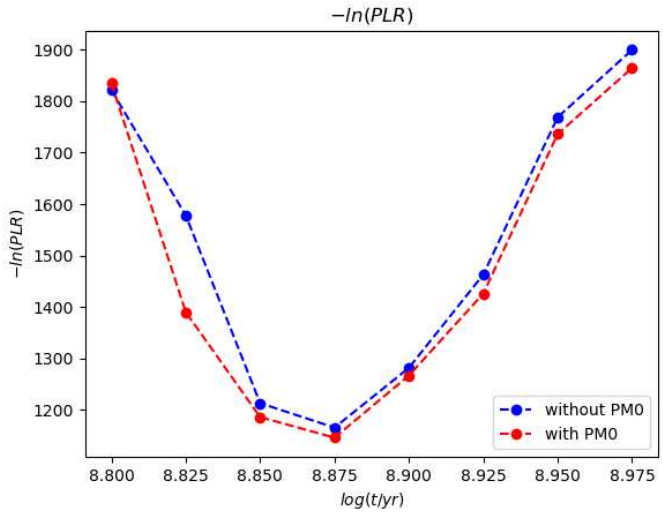

Figure 5.12: $-\ln \mathrm{PLR}$ as function of the age log(t/yr) for NGC 1831, for a metallicity of $Z = 0.007$. Blue points represent the $-\ln \mathrm{PLR}$ of the models computed without taking into account the PM_0 for the LMC field and MW foreground. Red points correspond to the case in which the PM_0 is taken into account when computing the best-fitting models.

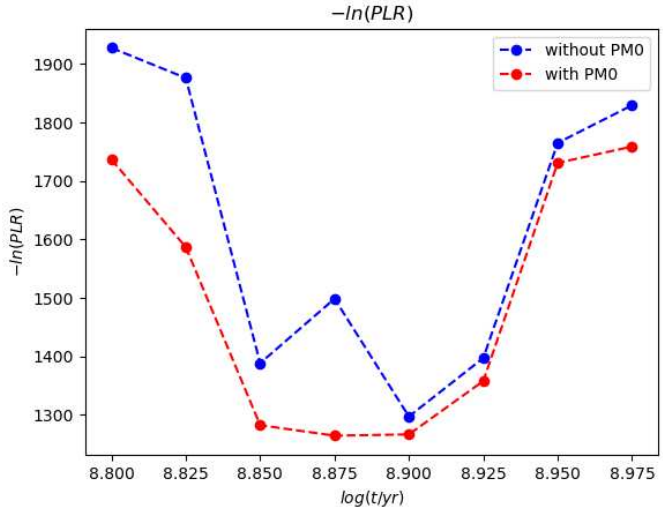

Figure 5.13: $-\ln \mathrm{PLR}$ as function of the age log(t/yr) for NGC 1831, for a metallicity of $Z = 0.008$. Blue points represent the $-\ln \mathrm{PLR}$ of the models computed without taking into account the PM_0 for the LMC field and MW foreground. Red points correspond to the case in which the PM_0 is taken into account when computing the best-fitting models.

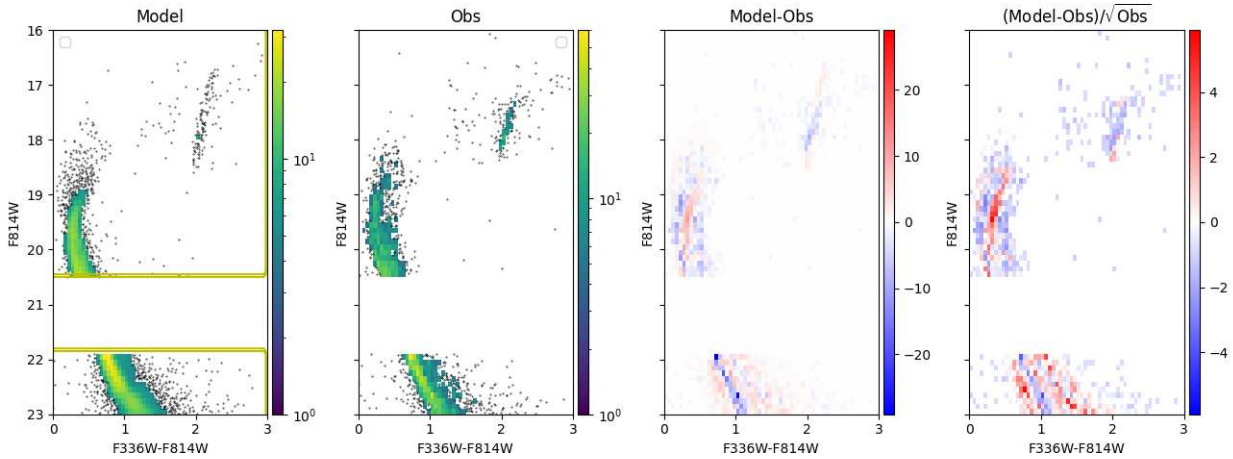

Figure 5.14: Left-hand panel: Hess diagram of the best-fitting model corresponding to a metallicity of $Z = 0.007$ and age $\log(t/yr) = 8.875$. Second panel: Hess diagram of the observation of NGC 1831 obtained with the UVIS-WFC3 of the HST. Third panel: residuals. Right-hand panel: normalized residuals.

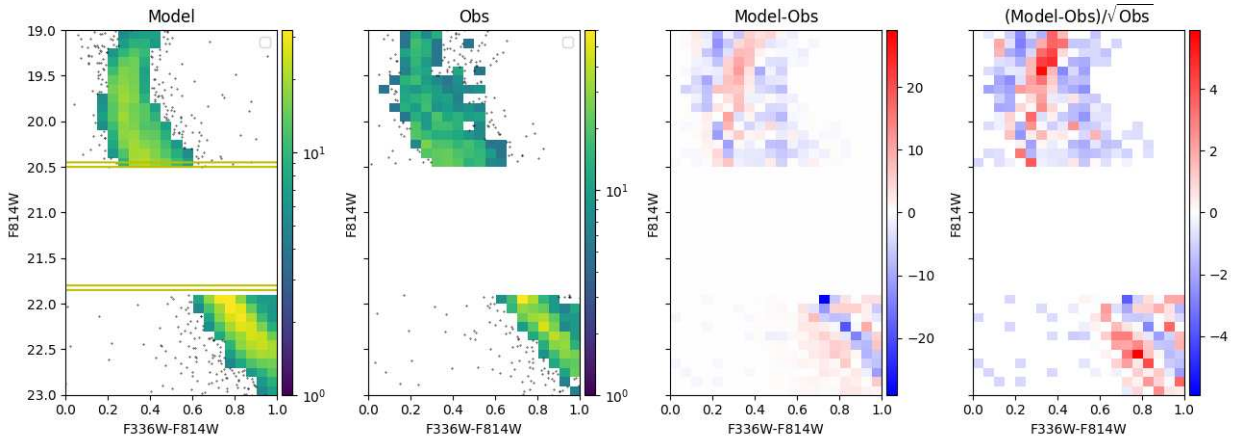

Figure 5.15: Same as Figure 5.14, but with a zoom on the MS region.

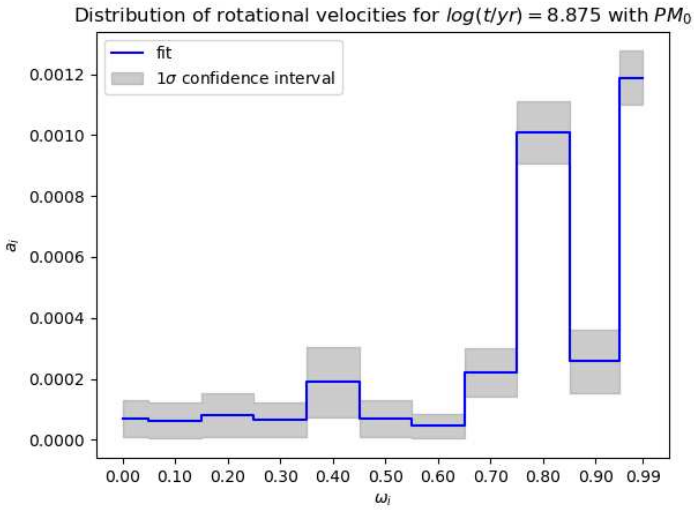

Figure 5.16: Plot of the best-fit values of the a_i coefficients for NGC 1831 as function of the initial rotation rate $\omega_{\rm i}$. Grey boxes represent the 1σ confidence interval.

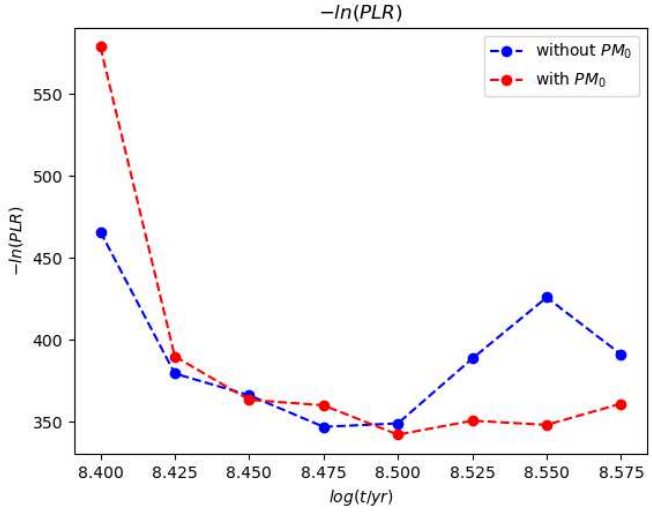

Figure 5.17: $-\ln$PLR as function of the age log(t/yr) for NGC 1866, for a metallicity of $Z = 0.006$. Blue points represent the $-\ln$PLR of the models computed without taking into account the PM_0 for the LMC field and MW foreground. Red points correspond to the case in which the PM_0 is taken into account when computing the best-fitting models.

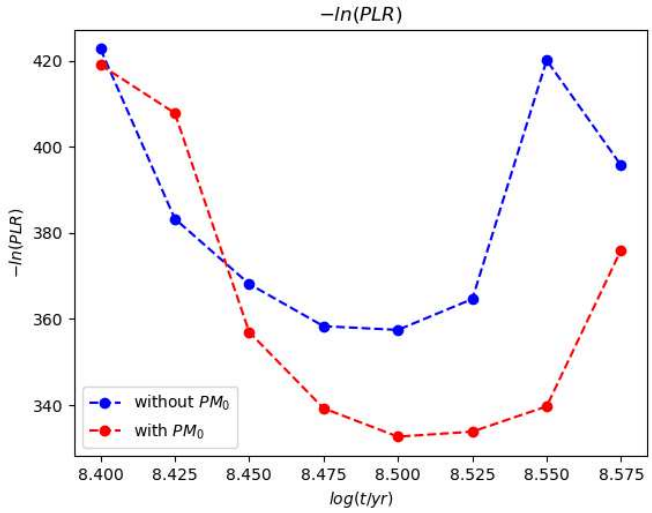

Figure 5.18: $-\ln \mathrm{PLR}$ as function of the age log(t/yr) for NGC 1866, for a metallicity of $Z = 0.007$. Blue points represent the $-\ln \mathrm{PLR}$ of the models computed without taking into account the PM_0 for the LMC field and MW foreground. Red points correspond to the case in which the PM_0 is taken into account when computing the best-fitting models.

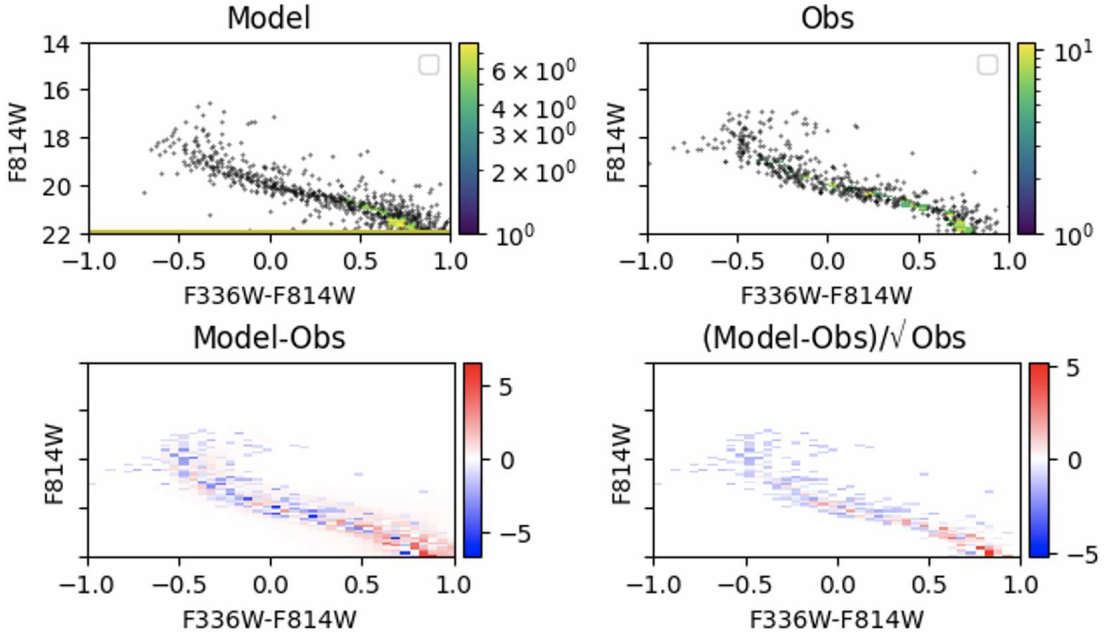

Figure 5.19: Left-hand panel: Hess diagram of the best-fitting model corresponding to a metallicity of $Z = 0.007$ and age log(t/yr) = 8.850. Second panel: Hess diagram of the observation of NGC 419 obtained with the ACS of the HST. Third panel: residuals. Right-hand panel: normalized residuals.

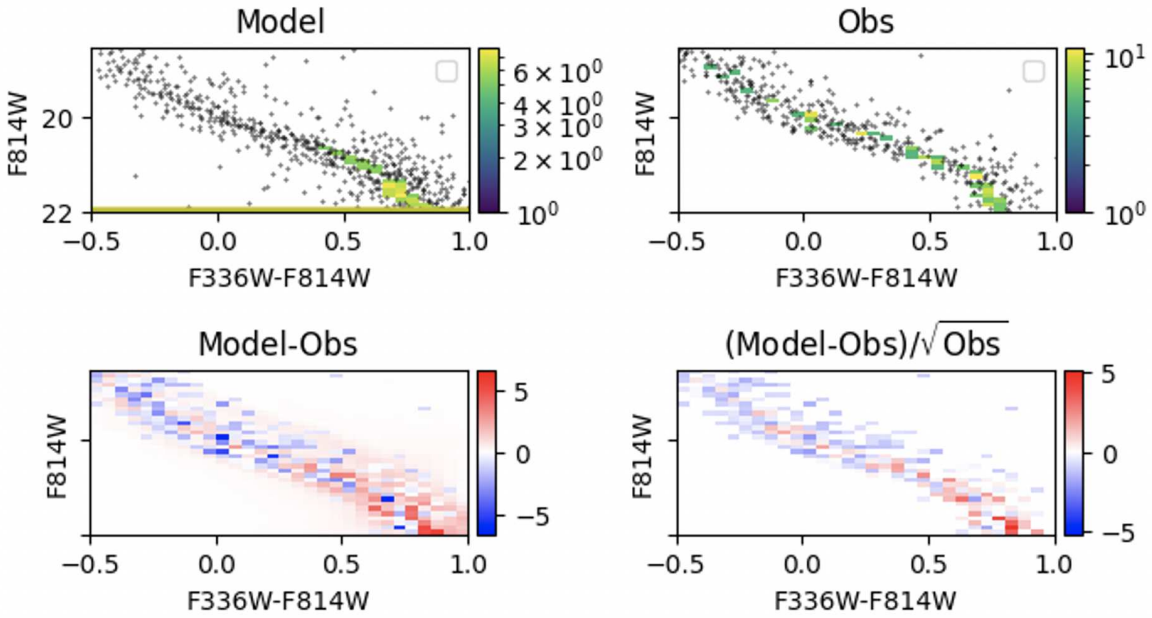

Figure 5.20: Same as Figure 5.19 but with a zoom on the split MS.

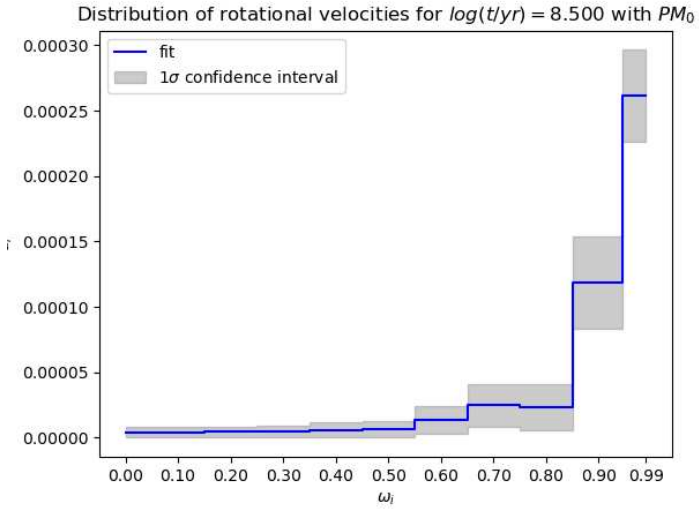

Figure 5.21: Plot of the best-fit values of the a_i coefficients for NGC 1866 as function of the initial rotation rate ω_i. Grey boxes represent the 1σ confidence interval.

Chapter 6

Conclusions

There has been growing evidence in recent years that star clusters in the MCs contain stars with a significant spread in rotation velocity. Indeed, the excellent photometry provided by the HST has revealed new surprises, such as the presence of structures which cannot be represented by evolutionary isochrones for a single age or metallicity in the observed CMDs of young and intermediate-age clusters of the MCs. These include the discovery of eMSTOs and split MS, or instances of clusters that exhibit a dual RC, as for example NGC 419. One of the first ideas proposed to explain this phenomenon was the "age spread scenario" (Mackey et al. (2008)), suggesting that each cluster might consist of at least two separate groups of stars with similar metal abundances but ages separated by up to $\sim$ 300 million years. However, it was only recently recognized, starting from the seminal paper by Bastian and De Mink (2009), that stellar rotation could be playing a crucial role in determining the photometric properties of stars born in populous star clusters in the MCs and in MW open clusters. The reduced gravity in rotating stars results in lower luminosities and effective temperatures. Additionally, the star's orientation relative to the observer's line of sight plays a significant role: a star deformed by fast rotation appears brighter and hotter if viewed pole-on. In addition, mixing processes induced by rotation modify the composition of the stellar envelope and effectively increase the size of the stellar core, resulting in higher luminosities and cooler temperatures for turn-off stars. These effects can significantly alter the colour and magnitude of stars, and therefore the CMD of a cluster (see Figure 2.4 and Figure 2.5).

In this thesis I delve into a comprehensive study of the stellar rotation distribution of four target clusters of the MCs through the application of models that are complete in all evolutionary phases and include rotation. The analysis concerns four clusters: NGC 419 of the SMC and NGC 2203, NGC 1831 and NGC 1866 of the LMC. All these objects are very rich in stars, and present all the interesting features associated with rotation in their CMDs.

Using isochrones derived from PARSEC V2.0 (Nguyen et al. (2022)) stellar tracks and

TRILEGAL (Girardi et al. (2005a)), the analysis begins by generating distinct stellar populations, each with a different rotation rate. The PAdova and tRieste Stellar Evolutionary Code (PARSEC) was initially introduced by Bressan et al. (2012), and it has subsequently been employed in various studies to construct extensive sets of stellar tracks and isochrones. In a more recent development, Costa et al. (2019) made significant progress in enhancing the code, incorporating the effects of rotation. This advancement resulted in the updated version, known as PARSEC V2.0 (Nguyen et al. (2022)). Isochrones for this work are then constructed with the TRILEGAL code (Girardi et al. (2005a)), which interpolates all the additional quantities needed to characterise rotating stars in the metallicity range between $Z = 0.004$ and 0.017, in the age range $7.0 \leq log(\mathrm{t/yr}) \leq 10.1$ and in the rotation rate range $0.0 \leq \omega_{\mathrm{i}} \leq 0.99$. Once isochrones are corrected for extinction and distance modulus, stellar populations are generated manually through linear interpolation, including binary systems and assuming a uniform distribution of the inclination angle. These stellar populations are referred to as "Partial Models" (PMs), and they are generated in form of Hess diagrams, which are matrix representations of the stellar density across the CMD. PMs are then fed to *sfhfinder* code (Mazzi et al. (2021)) to derive both the best-fitting solution that better represents the observed data and the confidence intervals of the fitted parameters. In particular, the final model is a linear combination of the PMs (see equation 4.2), telling us the relative importance of each population corresponding to each rotational velocity. Moreover, each final model also include the simulation for the background field of the LMC/SMC and for the MW foreground, labeled as PM_0.

For each cluster, it was decided to produce 11 Partial Models (corresponding to 11 values of the initial rotation rate $\omega_{\mathrm{i}} = 0.0, 0.1, 0.2, 0.3, 0.4, 0.5, 0.6, 0.7, 0.8, 0.9, 0.99$) for 2 values of the metallicity and 8 values of the age, resulting in a total amount of 16 best-fitting models M given by equation 4.2. Moreover, in order to infer the effect of including the PM_0 model for the MCs field and MW foreground, the 16 best-fitting models were computed both with and without the PM_0. Afterwards, given the poissonian nature of the distribution of our data, we chose to compute and minimize equation 4.17 as the most suitable approach to identify the best model among those 32 best-fitting models. In all cases the best-fitting model incorporating the PM_0 outperformed the best-fitting model with identical age and metallicity but lacking the PM_0. Table 6.1 summarizes the values of the age and metallicity of the best-fitting model suggested by the analysis for each cluster. The age of NGC 419 is estimated to be ~ 1.2 Gyr, younger with respect to the value assumed from literature (Goudfrooij et al. (2014)). The same holds for NGC 1831, for which the analysis suggests $t \sim 750$ Myr, about 50 Myr younger with respect to Correnti et al. (2021). On the other side the best-fit model for NGC 2203 suggests a value for the age that is perfectly in accordance with Goudfrooij et al. (2014). Finally, NGC 1866 is the only cluster of the analysis that is older with respect to the literature (Goudfrooij et al. (2018)).

One important aspect that is worth to mention is that, other than obtaining the distribution of rotational velocities, we chose to employ *sfhfinder* to fit the binary fraction

Table 6.1: Values of the age and metallicity of the best-fitting model suggested by the analysis for each cluster. Column 1: cluster name; Column 2: logarithm of the age of the best-fitting model (Gyr); Column 3: metallicity of the best-fitting model.

Cluster name	log(t/yr)	Z
NGC 419	9.075	0.003
NGC 2203	9.175	0.008
NGC 1831	8.875	0.007
NGC 1831	8.500	0.007

and the shifts in magnitude and colour as well, for each cluster. The first quantity provides insight into the amount of binary systems with respect to the total number of stars in the cluster. Notably, NGC 419 exhibits the highest count of binary systems ($f_{\rm bin} = 0.200$) among the objects in this study, while NGC 1866 displays the lowest count ($f_{\rm bin} = 0.085$). The shifts in magnitude and color, on the other hand, can be used to calculate the resulting distance and extinction following the fitting procedure. Indeed, when TRILEGAL isochrones are corrected before generating stellar populations, we assumed for each cluster a given value for the distance modulus $(m - M)_0$ and V-band extinction $A_{\rm v}$, that are listed in Table 3.1. Hence, for each cluster we assumed a given value for the apparent distance modulus in the F814W band:

$$(m - M)_{\rm F814W} = 5\log(d) - 5 + A_{\rm F814W} \tag{6.1}$$

where $A_{\rm F814W} = A_{\rm v} \cdot C_{\rm F814W}$, with $C_{\rm F814W}$ being available in the YBC tables (Chen et al. (2019)). It follows that, if we want to obtain the distance modulus resulting from the fit we should add ΔMag to the assumed apparent distance modulus. Moreover, the colour resulting after the fit is given by adding both ΔMag and ΔCol to the colour before the fit. Using this additional color excess and the apparent distance modulus, one can derive the distance and V-band extinction values obtained after the fitting process, denoted as d_2 and $A_{\rm v,2}$ respectively. These outcomes, together with the distance d_1 and V-band extinction $A_{\rm v,1}$ assumed before the fit, are listed in Table 6.2. In all cases, the cluster's calculated distance is slightly greater than the assumed value, and the V-band extinction also exhibits a higher value compared to the assumed one, except for NGC 1866.

The final results of this analysis are outlined in Chapter 5 and Figure 6.1 provides an overview of the stellar rotational velocity distribution within the clusters under investigation. The top panels show the velocity distribution of NGC 419 on the left and NGC 2203 on the right, while bottom pictures represent the velocity distribution of NGC 1831 (left) and NGC 1866 (right). NGC 419 appears to be primarily populated by stars featuring $\omega_{\rm i} > 0.90$, accompanied by an almost negligible presence of stars with $\omega_{\rm i} < 0.9$. Meanwhile, the velocity distribution of NGC 2203 displays a slight shift towards lower $\omega_{\rm i}$ values, with only a minimal number of stars with a rotation rate equal to the breakup value; nevertheless, $\omega_{\rm i}$ still maintains a value above 0.6. NGC 1831, on the other side, stands out as the only cluster where a discernible, although very small, group of stars

Table 6.2: Values for the distance and V-band extinction before and after the fit. Column 1: cluster name; Column 2: assumed distance before the fit in kpc; Column 3: distance resulting after the fit in kpc; Column 4: assumed V-band extinction before the fit; Column 5: V-band extinction resulting after the fit.

Cluster name	d_1	d_2	$A_{\mathrm{v},1}$	$A_{\mathrm{v},2}$
NGC 419	58.88	61.66	0.15	0.40
NGC 2203	47.21	48.53	0.16	0.35
NGC 1831	46.77	48.75	0.11	0.25
NGC 1866	48.53	51.05	0.28	0.22

exhibits $\omega_{\mathrm{i}} \lesssim 0.5$. However, the most abundant group in NGC 1831 consists of stars with $\omega_{\mathrm{i}} = 0.99$, and this trait similarly defines the rotational velocity distribution of NGC 1866. The latter only harbors stars with $\omega_{\mathrm{i}} > 0.6$, similarly to what happens for NGC 2203, but in contrast to it the distribution is peaked at higher velocities. Looking at the most recent literature regarding NGC 1866, the distribution of rotational velocities was expected to have a bimodal trend, accounting for the presence of slow-rotating blue MS stars and fast rotators belonging to the red MS. As anticipated in Section 5.4, the absence of slow rotators resulting from this work can most likely be attributed to the limited amount of data available for NGC 1866. Moreover, this discrepancy may be due to our choice to assume a unique value of the age for the PMs, while Costa et al. (2019) clearly shows an age difference of ~ 112 Myr between blue MS stars and red MS stars.

Ultimately, from this research I can conclude that the CMD morphology of young and intermediate-age MC clusters can be completely explained within the context of rapid and extreme rotation.

In the future, this analysis could be extended to a higher number of stellar clusters of the MCs with different age and metallicity in order to see whether the outcomes observed in this study hold as a general pattern within these two nearby irregular dwarf galaxies. In this perspective, it may be interesting to study more clusters with split MS and check if the analysis faces similar issues like those encountered in fitting NGC 1866. Moreover, this work could be expanded to young and intermediate-age clusters within the MW, providing a more comprehensive understanding of the underlying mechanisms shaping the CMDs in a different galactic environment.

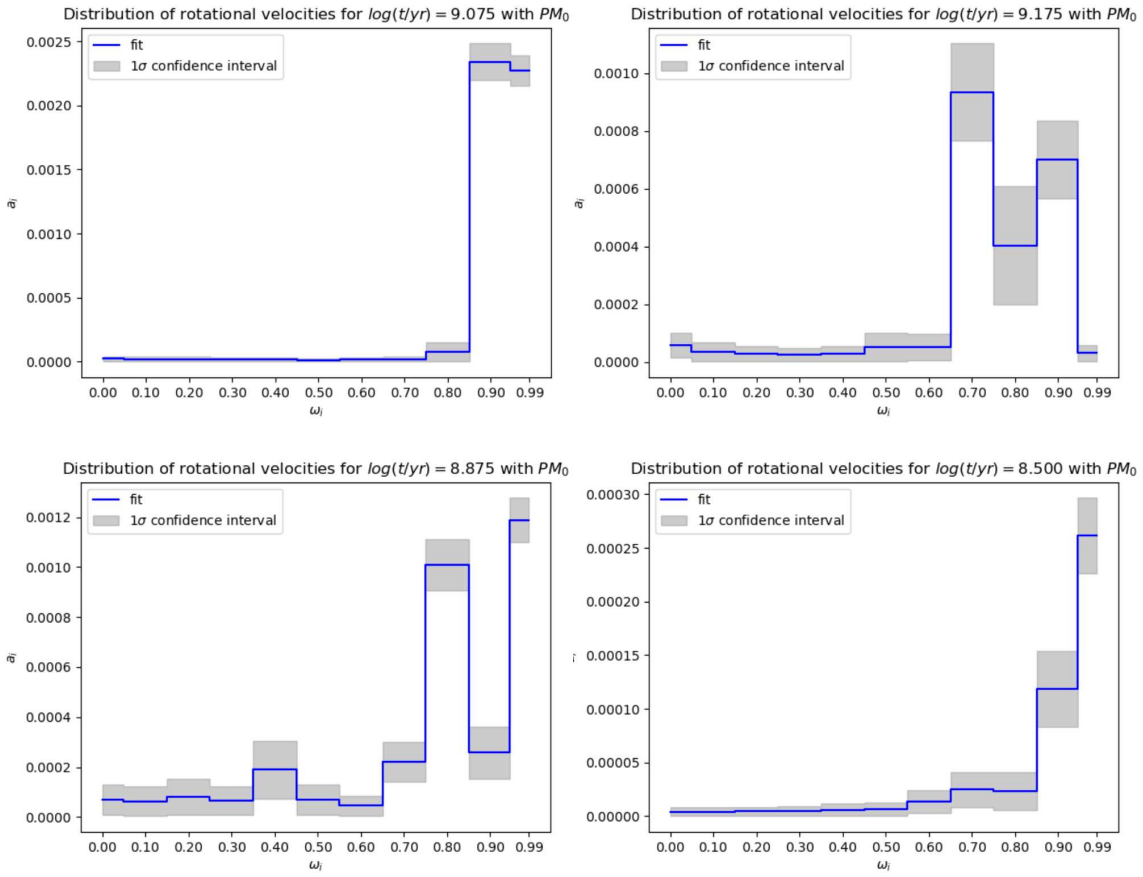

Figure 6.1: Distribution of stellar rotational velocities in NGC 419 (top left panel), NGC 2203 (top right panel), NGC 1831 (bottom left panel) and NGC 1866 (bottom right panel).

Ringraziamenti

Questa tesi rappresenta il culmine del mio percorso a Padova dopo sei lunghi anni e mi sembra giusto concluderlo con dei ringraziamenti.

Anzitutto ringrazio la professoressa Marigo e il professor Girardi per avermi proposto questo progetto che si è rivelato non solo interessante ma soprattutto un'opportunità stimolante che mi ha permesso di avere un'idea di cosa significhi fare ricerca. Vi ringrazio inoltre per aver capito, compreso e appoggiato il mio bisogno di riavvicinarmi a casa e di conseguenza lasciare Padova. Ringrazio il Dott. Mazzi Alessandro per la sua gentilezza e per la disponibilità che mi ha dimostrato sempre, a qualunque orario e in qualunque giorno gli scrivessi.

Il ringraziamento più grande va a mia mamma Maide, mio papà Pasquale, e ai miei fratelli Nicolò e Gloria. In sei anni mi avete aiutata con ogni mezzo possibile, non solo a livello economico ma soprattutto psicologicamente, rimanendomi accanto in ogni momento nonostante la distanza.

Ringrazio Fabrizio, Marco, Patrizia, Flavio, Erika, Linda, Nicola e Stefano e tutte le altre persone che mi hanno accompagnata in questa avventura. È stato bello condividere con voi le migliaia di emozioni che caratterizzano un percorso di studi e sono sicura che ricorderò questi anni per sempre. Un ulteriore ringraziamento va anche a Daniele, con cui ho condiviso questi ultimi sei mesi di università, seppure a distanza ma supportandoci a vicenda.

Un grazie anche alle mie "amiche di giù", Giordana, Silvia e Rebecca, amiche di una vita che seppur lontane mi sono sempre state vicine.

Dulcis in fundo, un grazie speciale va ad Antonio, che mi ha tenuto la mano fin dal terzo anno di università e ha avuto modo di vedere ogni sfaccettatura di questi anni. Il mio pessimismo è noto, ma tu sei sempre riuscito a illuminare le parti buie del mio percorso e rassicurarmi. La cosa più bella che potessi fare è stata ripetermi in continuazione quanto fossi fiero di me e non ti ringrazierò mai abbastanza.

Bibliography

Asplund, M., Grevesse, N., Sauval, A. J., and Scott, P. (2009). The chemical composition of the sun. *Annual Review of Astronomy and Astrophysics*, 47(1):481–522.

Bastian, N. and De Mink, S. E. (2009). The effect of stellar rotation on colour–magnitude diagrams: on the apparent presence of multiple populations in intermediate age stellar clusters. *Monthly Notices of the Royal Astronomical Society: Letters*, 398(1):L11–L15.

Bramich, D. M., Horne, K., Bond, I. A., Street, R. A., Collier Cameron, A., Hood, B., Cooke, J., James, D., Lister, T. A., Mitchell, D., Pearson, K., Penny, A., Quirrenbach, A., Safizadeh, N., and Tsapras, Y. (2005). A survey for planetary transits in the field of NGC 7789. , 359(3):1096–1116.

Bressan, A., Marigo, P., Girardi, L., Salasnich, B., Dal Cero, C., Rubele, S., and Nanni, A. (2012). PARSEC: stellar tracks and isochrones with the PAdova and TRieste Stellar Evolution Code. , 427(1):127–145.

Bruzual, A. G. (2009). Star clusters as simple stellar populations. *arXiv*, page arXiv:0911.0791.

Burleson, K. (2018). Uniform inclination. http://keatonb.github.io/archivers/uniforminclination.

Caffau, E., Ludwig, H. G., Steffen, M., Freytag, B., and Bonifacio, P. (2011). Solar Chemical Abundances Determined with a CO5BOLD 3D Model Atmosphere. , 268(2):255–269.

Chen, Y., Girardi, L., Fu, X., Bressan, A., Aringer, B., Dal Tio, P., Pastorelli, G., Marigo, P., Costa, G., and Zhang, X. (2019). YBC: a stellar bolometric corrections database with variable extinction coefficients. Application to PARSEC isochrones. , 632:A105.

Correnti, M., Goudfrooij, P., Bellini, A., and Girardi, L. (2021). The wide upper main sequence and main-sequence turnoff of the $\sim$ 800 Myr old star cluster NGC 1831. , 504(1):155–165.

Costa, G. (2019). Evolution of rotating stars with *PARSEC*: implementation and comparison with observations.

Costa, G., Girardi, L., Bressan, A., Chen, Y., Goudfrooij, P., Marigo, P., Rodrigues, T. S., and Lanza, A. (2019). Multiple stellar populations in NGC 1866. New clues from Cepheids and colour-magnitude diagram. , 631:A128.

Costa, G., Girardi, L., Bressan, A., Marigo, P., Rodrigues, T. S., Chen, Y., Lanza, A., and Goudfrooij, P. (2019). Mixing by overshooting and rotation in intermediate-mass stars. *Monthly Notices of the Royal Astronomical Society*, 485(4):4641–4657.

D'Antona, F., Montalbán, J., Kupka, F., and Heiter, U. (2002). The Böhm-Vitense Gap: The Role of Turbulent Convection. , 564(2):L93–L96.

de Juan Ovelar, M., Gossage, S., Kamann, S., Bastian, N., Usher, C., Cabrera-Ziri, I., Dotter, A., Conroy, C., and Lardo, C. (2019). Extended main sequence turnoffs in open clusters as seen by igaia/i – II. the enigma of NGC 2509. *Monthly Notices of the Royal Astronomical Society*, 491(2):2129–2136.

Decressin, T., Meynet, G., Charbonnel, C., Prantzos, N., and Ekström, S. (2007). Fast rotating massive stars and the origin of the abundance patterns in galactic globular clusters. *Astronomy &amp Astrophysics*, 464(3):1029–1044.

Denissenkov, P. A. and Hartwick, F. D. A. (2013). Supermassive stars as a source of abundance anomalies of proton-capture elements in globular clusters. *Monthly Notices of the Royal Astronomical Society: Letters*, 437(1):L21–L25.

D'Ercole, A., Vesperini, E., D'Antona, F., McMillan, S. L. W., and Recchi, S. (2008). Formation and dynamical evolution of multiple stellar generations in globular clusters. *Monthly Notices of the Royal Astronomical Society*, 391(2):825–843.

Dolphin, A. E. (2002). Numerical methods of star formation history measurement and applications to seven dwarf spheroidals. , 332(1):91–108.

Dotter, A., Chaboyer, B., Jevremović , D., Baron, E., Ferguson, J. W., Sarajedini, A., and Anderson, J. (2007). The ACS survey of galactic globular clusters. II. stellar evolution tracks, isochrones, luminosity functions, and synthetic horizontal-branch models. *The Astronomical Journal*, 134(1):376–390.

D'Antona, F., Milone, A., Tailo, M., Ventura, P., Vesperini, E., and Di Criscienzo, M. (2017). Stars caught in the braking stage in young Magellanic Cloud clusters. *Nat Astron 1, 0186.*

Ekström, S., Meynet, G., Georgy, C., and Granada, A. (2018). Stellar rotation and its importance in the interpretation of stellar populations in MCs. *SAIt*, 89, 50.

Espinosa Lara, F. and Rieutord, M. (2011). Gravity darkening in rotating stars. *Astronomy &amp Astrophysics*, 533:A43.

Georgy, C., Charbonnel, C., Amard, L., Bastian, N., Ekström, S., Lardo, C., Palacios, A., Eggenberger, P., Cabrera-Ziri, I., Gallet, F., and Lagarde, N. (2019). Disappearance of the extended main sequence turn-off in intermediate age clusters as a consequence of magnetic braking. *A&A*, 622:A66.

Gim, M., Vandenberg, D. A., Stetson, P. B., Hesser, J. E., and Zurek, D. R. (1998). The Open Cluster NGC 7789. II. CCD VI Photometry. , 110(753):1318–1335.

Girardi, L. (2016). Red Clump Stars. , 54:95–133.

Girardi, L., Bertelli, G., Bressan, A., Chiosi, C., Groenewegen, M. A. T., Marigo, P., Salasnich, B., and Weiss, A. (2002). Theoretical isochrones in several photometric systems. I. Johnson-Cousins-Glass, HST/WFPC2, HST/NICMOS, Washington, and ESO Imaging Survey filter sets. , 391:195–212.

Girardi, L., Costa, G., Chen, Y., Goudfrooij, P., Bressan, A., Marigo, P., and Bellini, A. (2019). On the photometric signature of fast rotators. *Monthly Notices of the Royal Astronomical Society*, 488(1):696–705.

Girardi, L., Groenewegen, M. A. T., Hatziminaoglou, E., and da Costa, L. (2005a). Star counts in the Galaxy. Simulating from very deep to very shallow photometric surveys with the TRILEGAL code. , 436(3):895–915.

Girardi, L., Groenewegen, M. A. T., Hatziminaoglou, E., and da Costa, L. (2005b). Star counts in the Galaxy. Simulating from very deep to very shallow photometric surveys with the TRILEGAL code. , 436(3):895–915.

Girardi, L., Rubele, S., and Kerber, L. (2009). Discovery of two distinct red clumps in NGC 419: a rare snapshot of a cluster at the onset of degeneracy. , 394(1):L74–L78.

Girardi, L., Rubele, S., and Kerber, L. (2010). Star clusters with dual red clumps. In de Grijs, R. and Lépine, J. R. D., editors, *Star Clusters: Basic Galactic Building Blocks Throughout Time and Space*, volume 266, pages 320–325.

Glatt, K., Grebel, E. K., Sabbi, E., Gallagher, John S., I., Nota, A., Sirianni, M., Clementini, G., Tosi, M., Harbeck, D., Koch, A., Kayser, A., and Da Costa, G. (2008). Age Determination of Six Intermediate-Age Small Magellanic Cloud Star Clusters with HST/ACS. , 136(4):1703–1727.

Gossage, S., Conroy, C., Dotter, A., Cabrera-Ziri, I., Dolphin, A. E., Bastian, N., Dalcanton, J. J., Goudfrooij, P., Johnson, L. C., Williams, B. F., Rosenfield, P., Kalirai, J., and Fouesneau, M. (2019). Combined Effects of Rotation and Age Spreads on Extended Main-Sequence Turn Offs. , 887(2):199.

Goudfrooij, P., Girardi, L., Bellini, A., Bressan, A., Correnti, M., and Costa, G. (2018). The Minimum Mass of Rotating Main-sequence Stars and its Impact on the Nature of Extended Main-sequence Turnoffs in Intermediate-age Star Clusters in the Magellanic Clouds. *The Astrophysical Journal Letters*, 864(1):1–6.

Goudfrooij, P., Girardi, L., Kozhurina-Platais, V., Kalirai, J. S., Platais, I., Puzia, T. H., Correnti, M., Bressan, A., Chandar, R., Kerber, L., Marigo, P., and Rubele, S. (2014). Extended Main Sequence Turnoffs in Intermediate-age Star Clusters: A Correlation between Turnoff Width and Early Escape Velocity. , 797(1):35.

Gratton, R., Bragaglia, A., Carretta, E., D'Orazi, V., Lucatello, S., and Sollima, A. (2019). What is a globular cluster? An observational perspective. , 27(1):8.

Kippenhahn, R., Meyer-Hofmeister, E., and Thomas, H. C. (1970). Rotation in Evolving Stars. , 5:155.

Mackey, A. D., Broby Nielsen, P., Ferguson, A. M. N., and Richardson, J. C. (2008). Multiple Stellar Populations in Three Rich Large Magellanic Cloud Star Clusters. , 681(1):L17.

Marino, A. F., Przybilla, N., Milone, A. P., Costa, G. D., D'Antona, F., Dotter, A., and Dupree, A. (2018). Different stellar rotations in the two main sequences of the young globular cluster NGC 1818: The first direct spectroscopic evidence. *The Astronomical Journal*, 156(3):116.

Marino, A. F., Villanova, S., Milone, A. P., Piotto, G., Lind, K., Geisler, D., and Stetson, P. B. (2011). SODIUM–OXYGEN ANTICORRELATION AMONG HORIZONTAL BRANCH STARS IN THE GLOBULAR CLUSTER m4. *The Astrophysical Journal*, 730(2):L16.

Marino, A. F., Villanova, S., Piotto, G., Milone, A. P., Momany, Y., Bedin, L. R., and Medling, A. M. (2008). Spectroscopic and photometric evidence of two stellar populations in the galactic globular cluster ngc 6121 (m4. *A&A*, 490(2):625–640.

Mazzi, A., Girardi, L., Zaggia, S., Pastorelli, G., Rubele, S., Bressan, A., Cioni, M.-R. L., Clementini, G., Cusano, F., Rocha, J. P., Gullieuszik, M., Kerber, L., Marigo, P., Ripepi, V., Bekki, K., Bell, C. P. M., de Grijs, R., Groenewegen, M. A. T., Ivanov, V. D., Oliveira, J. M., Sun, N.-C., and van Loon, J. T. (2021). The VMC survey - XLIII. The spatially resolved star formation history across the Large Magellanic Cloud. , 508(1):245–266.

Meynet, G. and Maeder, A. (1997). Stellar evolution with rotation. I. The computational method and the inhibiting effect of the μ-gradient. , 321:465–476.

Milone, A. P. and Marino, A. F. (2022). Multiple populations in star clusters.

Milone, A. P., Marino, A. F., D'Antona, F., Bedin, L. R., Da Costa, G. S., Jerjen, H., and Mackey, A. D. (2016). Multiple stellar populations in Magellanic Cloud clusters – IV. The double main sequence of the young cluster NGC 1755. *Monthly Notices of the Royal Astronomical Society*, 458(4):4368–4382.

Milone, A. P., Marino, A. F., Piotto, G., Bedin, L. R., Anderson, J., Aparicio, A., Bellini, A., Cassisi, S., D'Antona, F., Grundahl, F., Monelli, M., and Yong, D. (2013). A WFC3/HST View of the Three Stellar Populations in the Globular Cluster NGC 6752. , 767(2):120.

Milone, A. P., Piotto, G., Bedin, L. R., Aparicio, A., Anderson, J., Sarajedini, A., Marino, A. F., Moretti, A., Davies, M. B., Chaboyer, B., Dotter, A., Hempel, M., Marí n-Franch, A., Majewski, S., Paust, N. E. Q., Reid, I. N., Rosenberg, A., and Siegel, M. (2012). The ACS survey of galactic globular clusters. *Astronomy &amp Astrophysics*, 540:A16.

Nguyen, C. T., Costa, G., Girardi, L., Volpato, G., Bressan, A., Chen, Y., Marigo, P., Fu, X., and Goudfrooij, P. (2022). PARSEC V2.0: Stellar tracks and isochrones of low- and intermediate-mass stars with rotation. , 665:A126.

Overbeek, J. C., Friel, E. D., Jacobson, H. R., Johnson, C. I., Pilachowski, C. A., and Mészáros, S. (2014). Ngc 7789: An open cluster case study. *The Astronomical Journal*, 149(1):15.

Tio, P. D., Mazzi, A., Girardi, L., Barbieri, M., Zaggia, S., Bressan, A., Chen, Y., Costa, G., and Marigo, P. (2021). Dissecting the igaia/i HR diagram within 200 pc. *Monthly Notices of the Royal Astronomical Society*, 506(4):5681–5697.

von Zeipel, H. (1924). The radiative equilibrium of a rotating system of gaseous masses. , 84:665–683.